

Article

Mineral Assemblage of Olivine-Hosted Melt Inclusions in a Mantle Xenolith from the V. Grib Kimberlite Pipe: Direct Evidence for the Presence of an Alkali-Rich Carbonate Melt in the Mantle Beneath the Baltic Super-Craton

Alexander V. Golovin ^{1,2}, Alexey A. Tarasov ^{1,3} and Elena V. Agasheva ^{1,*}

¹ V.S. Sobolev Institute of Geology and Mineralogy, Siberian Branch Russian Academy of Sciences, 630090 Novosibirsk, Russia; avg@igm.nsc.ru (A.V.G.); tarasov.alexey@igm.nsc.ru (A.A.T.)

² Institute of the Earth's Crust, Siberian Branch Russian Academy of Science, 664033 Irkutsk, Russia

³ Department of Geology and Geophysics, Novosibirsk State University, 630090 Novosibirsk, Russia

* Correspondence: shchukinalena@igm.nsc.ru

Abstract: This report deals with the first mineralogical examination of secondary crystallized melt inclusions (CMIs) in healed cracks within olivine in a mantle peridotite xenolith from the V. Grib kimberlite pipe (Arkhangelsk diamondiferous province). In contrast to micro/nano-inclusions in diamonds, the studied CMIs are quite large (up to 50 μm), so that the mineral composition of the CMIs can be determined via conventional analytical approaches, e.g., Raman spectroscopy and scanning electron microscopy. Garnet peridotite is a coarse-grained mantle rock that equilibrates at 3.3 GPa and 750 °C (corresponding to a depth of ~100 km). The CMIs are therefore tiny snapshots of melt that existed in the shallow lithospheric mantle and were entrapped in olivine. In total, nineteen mineral species were identified among the daughter magmatic minerals of the CMIs. Various Na-K-Ca-, Na-Ca-, Na-Mg-, Ca-Mg-, Mg- and Ca-carbonates; Na-Mg-carbonates with the additional anions Cl^- , SO_4^{2-} and PO_4^{3-} ; alkali sulfates; chlorides; phosphates; sulfides; oxides; and silicates were established. Within the mineral assemblage, carbonates were predominant, with their abundance being more than 62 vol.%. The CMIs contained twelve alkali-rich minerals; nine of them were Na-bearing and showed bulk molar $(\text{Na} + \text{K})/\text{Ca} \geq 1$. The CMIs' parental melt was an alkali-rich carbonate liquid that contained low amounts of SiO_2 (≤ 9.6 wt%) and H_2O (≤ 2.6 wt%). According to our estimates, the time of complete equilibration between olivine within the healed cracks and host olivine in the mantle at the calculated P-T parameters for the studied xenolith should be no more than several years. Based on this geologically short time span, a genetic link between the studied CMIs and the magmatism that formed the V. Grib kimberlite pipe is suggested.

Keywords: melt inclusions; alkaline carbonates; carbonate mantle melts; mantle xenoliths; kimberlite; metasomatism; serpentinization; Baltic super-craton; V. Grib kimberlite pipe



Citation: Golovin, A.V.; Tarasov, A.A.; Agasheva, E.V. Mineral Assemblage of Olivine-Hosted Melt Inclusions in a Mantle Xenolith from the V. Grib Kimberlite Pipe: Direct Evidence for the Presence of an Alkali-Rich Carbonate Melt in the Mantle Beneath the Baltic Super-Craton. *Minerals* **2023**, *13*, 645. <https://doi.org/10.3390/min13050645>

Academic Editor: Alfons M. Van den Kerkhof

Received: 16 April 2023

Revised: 29 April 2023

Accepted: 4 May 2023

Published: 6 May 2023



Copyright: © 2023 by the authors. Licensee MDPI, Basel, Switzerland. This article is an open access article distributed under the terms and conditions of the Creative Commons Attribution (CC BY) license (<https://creativecommons.org/licenses/by/4.0/>).

1. Introduction

When reconstructing the evolution of the silicate lithospheric mantle of ancient cratons, a crucial role in metasomatic events leading to the transformation of previously depleted rocks is predominantly attributed to silicate-rich melts of various compositions (e.g., [1–14]). Compared to the effects of silicate metasomatism, direct evidence for the presence of carbonate or carbonate-rich melts in the continental lithosphere is less widespread. Some examples include the occurrence of (1) epigenetic carbonates in the interstitial space of mantle xenoliths from kimberlites [13,15–17], (2) carbonates texturally equilibrated with silicate minerals in so-called melt pockets in mantle xenoliths from kimberlites [13,14] and (3) carbonates in polymineralic inclusions in garnet and clinopyroxene megacrysts/xenocrysts from kimberlites (e.g., reviews in [18–20]). On the other hand, cryptic metasomatism (i.e.,

a more subtle type of metasomatism that results in geochemical modifications of mantle assemblages without the formation of new phases) of minerals from mantle rocks by carbonate melts has been recorded at various locations worldwide and is addressed in a significant number of publications (e.g., [8,21–26]).

Numerous studies of melt/fluid micro- and nano-inclusions in lithospheric fibrous diamonds the world over (e.g., [27–35]), including cuboid-type diamonds from the V. Grib kimberlite pipe [36], indicate a significant role of local carbonate/alkaline–carbonate melts/fluids in the formation of these diamonds. Crystalline inclusions of carbonates in lithospheric diamonds are mainly calcite, magnesite and dolomite, which are considered rare compared with inclusions of silicate minerals (e.g., reviews in [37,38]). However, the volume of mineralogical data on carbonate mineral inclusions in lithospheric diamonds is constantly increasing. For instance, a polycrystalline inclusion consisting of bütschliite (carbonate polymorph with the crystal–chemical formula $K_2Ca(CO_3)_2$), eitelite ($Na_2Mg(CO_3)_2$) and dolomite ($CaMg(CO_3)_2$) has been recently found in the central part of a gem-quality diamond of lithospheric origin from the Sytykanskaya kimberlite pipe (Siberian craton) [39]. A high-pressure $CaCO_3$ polymorph, aragonite, was diagnosed in a sublithospheric diamond from the Komsomolskaya kimberlite pipe (Siberian craton) [40]. The latter finding indicates the possibility of diamond crystallization within the mantle substrate at depths below 300 km. Sublithospheric diamonds from the Juina area (Brazil) enclose crystallized micro- and nano-inclusions of a carbonatitic-type mineral paragenesis including carbonates (calcite, dolomite, nyerereite, nahcolite, magnesite and eitelite) and halides ($NaCl$, KCl , $CaCl_2$ and $PbCl_2$) [41–46]. It is believed that the crystallization medium for these diamonds was the initial carbonatitic melt which may have originated at depths corresponding to the lower transition zone or even the lower mantle. During ascent, this carbonate liquid dissociated into two immiscible parts: a carbonate–silicate and a chloride–carbonate melt. According to [42–46], the chloride–carbonate melt is parental to the observed natrocarbonatitic lower-mantle association.

Numerous experimental works have shown that at P-T parameters of the lithospheric mantle, carbonate/alkaline–carbonate melts can be in equilibrium or in partial equilibrium with various mantle mineral assemblages (e.g., [47–56]). It is currently accepted that these melts can be generated by low degrees of partial melting of mantle rocks (e.g., [24,57–63]).

Carbonate melts display unique physical properties, such as the lowest viscosities among known terrestrial melts, high mobility and wettability (e.g., [63]). Hence, carbonatitic melts may be highly effective metasomatic agents in the lithospheric mantle, as their low viscosity and high mobility permit percolation along grain boundaries of silicates over a large distance (e.g., [64]). Snapshots of such melts (primary melt inclusions in minerals of mantle rocks) were discovered even in samples from the shallow lithospheric mantle (~110–115 km), above the diamond stability field [65].

At present, large-scale occurrences of carbonatite magmatism on ancient cratons are unknown. However, kimberlite occurrences on ancient cratons are numerous, with the bulk composition of these rocks being ultramafic, generally poor in SiO_2 (up to 35 wt%, e.g., [66]). Based on the study of secondary melt inclusions in olivine from mantle xenoliths [67–72], as well as primary and pseudosecondary inclusions in kimberlite minerals (e.g., [20,67,73–84]), it is assumed that both primitive (inclusions in olivine of mantle xenoliths) and evolving-during-ascent (inclusions in minerals of kimberlites) kimberlite melts had an alkaline–carbonate composition.

These lines of evidence indicate that not only silicate, but also alkaline–carbonate and carbonate liquids play a significant role in lithospheric and sublithospheric processes beneath ancient cratons.

Melt inclusions in minerals of mantle xenoliths from basalts have been examined in at least several hundred publications (e.g., reviews in [85–88]), whereas those from kimberlites have received limited attention. In mantle xenoliths from kimberlites, melt inclusions in olivine have been investigated only in a particular type of the deepest mantle xenoliths—so-called sheared peridotites. At the same time, such studies of sheared peri-

dotites were carried out for only three kimberlite occurrences, namely for kimberlites of the Udachnaya and Komsomolskaya–Magnitnaya pipes (Siberian craton) and the Bultfontein pipe (Kaapvaal craton) [67–72].

This report presents the first results of a study aiming to characterize secondary crystallized melt inclusions in a granular xenolith from kimberlites, as well as to inspect poorly studied melt inclusions in kimberlite-borne mantle cargo of the Kola craton (part of the Baltic super-craton or East European platform). Both unexposed and exposed-on-the-surface crystallized melt inclusions have been examined using Raman- and electron-microprobe-based analytical techniques. In the discussion section, we show that the composition of the investigated melt inclusions provides direct evidence for the existence of alkali-carbonate Cl-S-P-bearing melt(s) in the shallow lithospheric mantle (≤ 100 km) beneath the Baltic super-craton.

2. Terminology and Definitions

Secondary melt inclusions are inclusions that originate within cracks in the host mineral during the following processes: (i) cracking of the host mineral, (ii) melt infiltration into the cracks and (iii) reaction of the host mineral matrix with the melt, necking down and formation of tiny portions of the melt within cracks. *Crystallized melt inclusions (CMI)*s are produced by the crystallization of the captured melt during cooling with the formation of a number of daughter minerals.

Daughter minerals are crystalline phases that precipitate (crystallize) from the original liquid (melt or fluid) after entrapment.

Carbonatite and carbonatite/carbonate melts. According to the IUGS systematics, carbonatites are rocks containing >50 vol.% primary (i.e., magmatic) carbonate minerals. The definition of carbonatite additionally stipulates that the rocks should contain <20 wt% SiO_2 . If a rock contains >20 wt% SiO_2 , it is recommended to refer to it as silicocarbonatite [89]. However, some researchers [90] are prone to use the term carbonatite in a wider sense to denote a rock containing >30 vol.% primary magmatic carbonates regardless of SiO_2 concentration. The liquids from which carbonatites crystallize are usually called carbonate-rich, or carbonate or carbonatite melts. Unfortunately, we are not aware of any universally accepted constraints on the concentrations of the dominant volatile component, CO_2 , in these compositionally diverse melts.

Primary kimberlite melts are melts that occurred in equilibrium (or partial equilibrium) with mantle rocks at the basement of the continental lithosphere.

Primitive kimberlite melts are melts that have insignificantly evolved when interacting with lithospheric mantle silicates during ascent to the surface (i.e., the composition of these melts is close to that of the primary ones).

Kimberlite magma is a melt (or melts, if immiscible) with some amounts of xenocrysts, xenoliths and liquidus phases.

3. Geological Background and Sample Description

The highly diamondiferous V. Grib kimberlite pipe is located within the Devonian–Upper Carboniferous (390–340 Ma; [91,92]) Arkhangelsk diamondiferous province (ADP) in the northern part of the Baltic super-craton (Figure 1). Compared to other ADP kimberlites, which contain extremely altered mantle xenoliths, the V. Grib kimberlite pipe comprises abundant weakly altered mantle xenoliths and their fragments [25,93,94]. Based on major- and trace-element composition, the V. Grib kimberlites belong to the moderate-titanium ($\text{TiO}_2 = 0.8\text{--}2.0$ wt%) group of ADP kimberlites [95,96]. The age of the V. Grib kimberlite emplacement was constrained at 372 ± 8 Ma (bulk-rock kimberlite analyses using the Rb-Sr dating technique [91]) and 376 ± 3 Ma (Rb-Sr dating of kimberlitic phlogopite [92]). The comprehensive data on the ADP magmatic bodies, including location, morphology, size, structure and composition, can be found in [92,97,98]. The detailed petrographic and geochemical data of the V. Grib kimberlites are presented in [95,96,99].

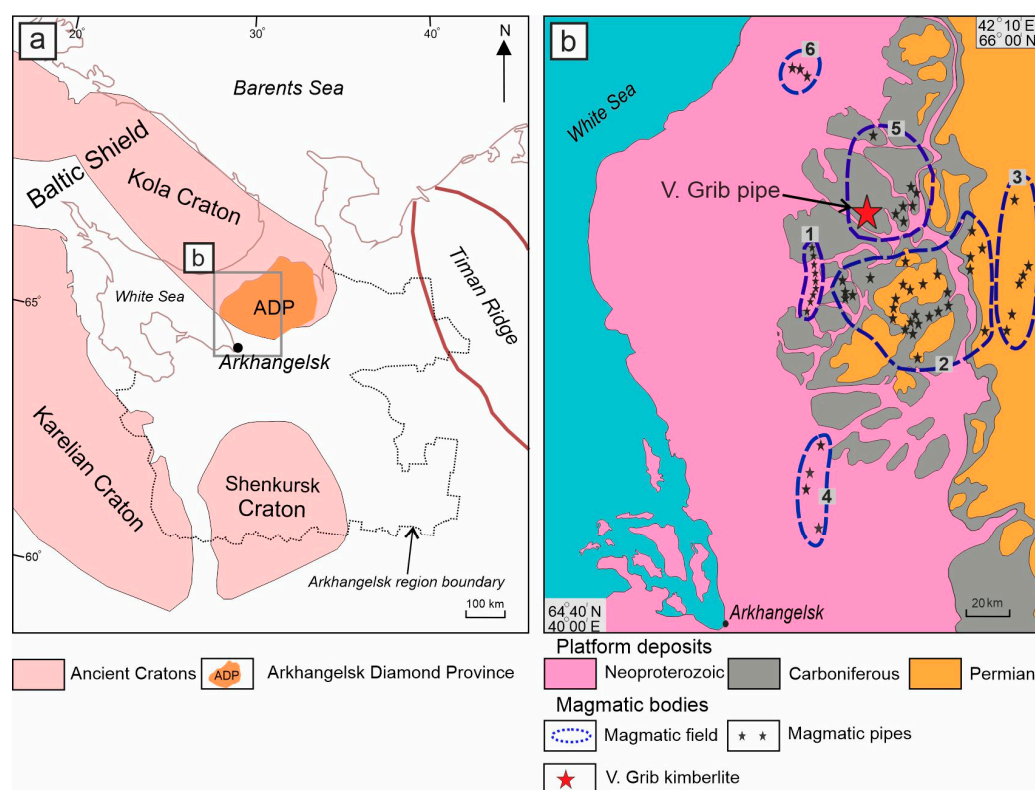


Figure 1. (a) Tectonic scheme of the northern part of the Baltic super-craton showing the location of Arkhangelsk Diamond Province (ADP), after [100,101]. (b) Location of the V. Grib kimberlite on the geological map of the ADP. Numbers indicate magmatic fields: 1—Zolotitsa, 2—Kepino, 3—Tur'ino, 4—Izhmozero, 5—Verkhotina, 6—Mela.

The studied sample, G1-25, is protogranular garnet peridotite. Table 1 provides summary data on this rock, including composition of major minerals and P-T calculation results.

Table 1. Electron microprobe data on rock-forming minerals (wt%) and P-T-depth estimates for garnet lherzolite xenolith (sample G1-25).

Element/Mineral	Ol	Opx	Grt	Cpx
SiO ₂	40.62	57.67	41.64	53.92
TiO ₂	n.a.	0.09	0.12	0.18
Al ₂ O ₃	n.a.	0.73	20.38	2.13
Cr ₂ O ₃	0.02	0.34	4.39	2.17
FeO _t	7.80	4.95	8.54	2.13
MnO	0.09	0.13	0.45	0.06
MgO	50.71	35.84	18.64	15.84
CaO	b.d.l.	0.25	5.38	20.59
Na ₂ O	n.a.	0.06	0.02	2.09
K ₂ O	n.a.	b.d.l.	0.01	0.02
NiO	0.40	n.a.	n.a.	n.a.
Total	99.62	100.04	99.56	99.13
Mg#	92.1	92.8	79.6	93.0
P, GPa			3.27	
T, °C			749	
Depth, km			100	

Representative analyzes are shown. n.a.—not analyzed. b.d.l.—below detection limit. Mg# in Ol = $100 \times \text{Mg}/(\text{Mg} + \text{Fe})$ (at.%) in olivine; Mg# in Opx = $100 \times \text{Mg}/(\text{Mg} + \text{Fe})$ (at.%) in orthopyroxene; P-T estimates were obtained using the two-pyroxene thermometer TA₉₈ [102] and orthopyroxene (Al-in-Opx) barometer NC₈₅ [103]. Ol—olivine, Opx—orthopyroxene, Cpx—clinopyroxene, Grt—garnet. Depth (km) calculation according to [104].

The peridotite is composed of predominant olivine (~80–84 vol.%) with subsidiary orthopyroxene (~6 vol.%), garnet (~5 vol.%) and clinopyroxene, with the latter showing variable modes across different thin sections (from <1 to ~5 vol.%). Phlogopite and chromite occur in minor volume proportions (Figure 2a,b). The peridotite is partly (~20 vol.%) altered by serpentine, which occurs around grains of olivine and orthopyroxene, and develops along cracks crosscutting these silicates. The rock-forming minerals are nevertheless well-preserved.

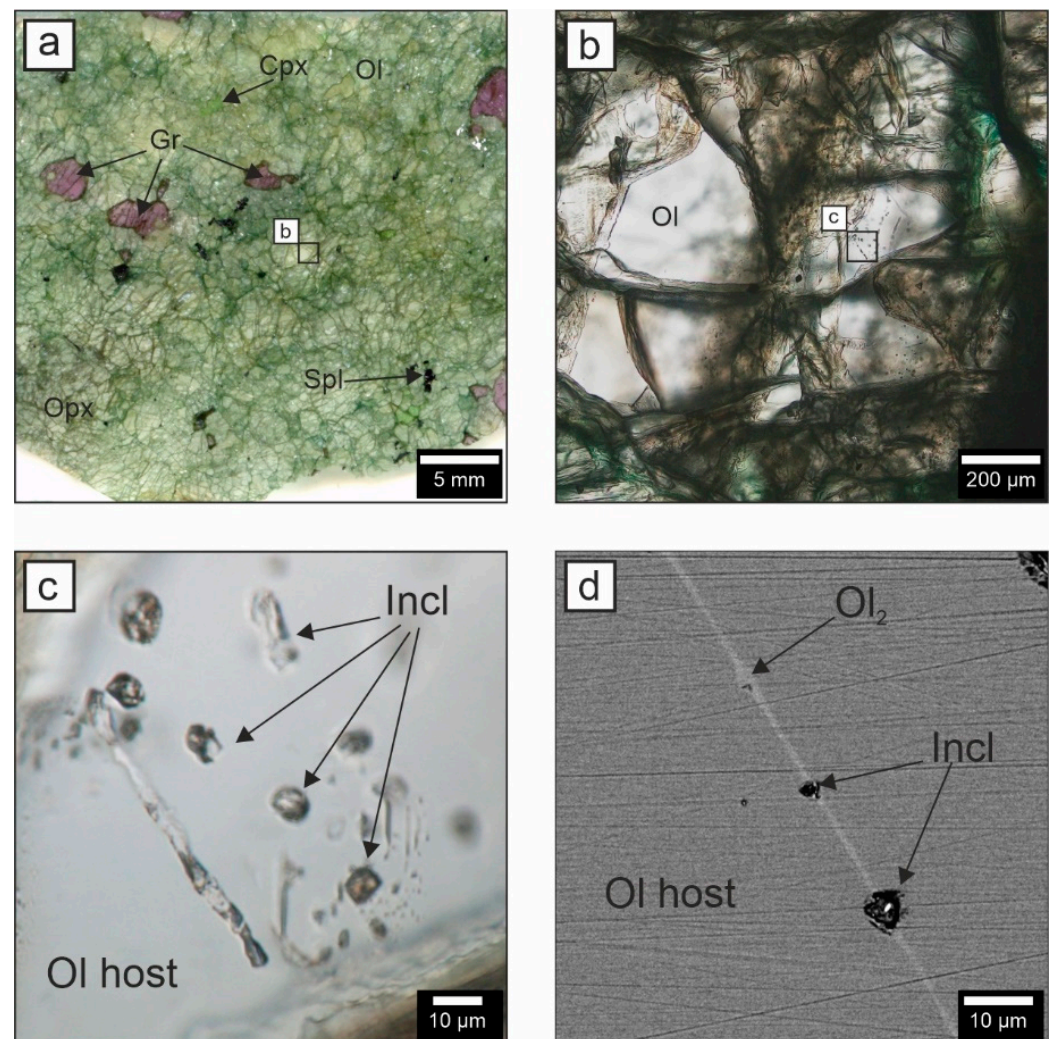


Figure 2. (a) Photomicrograph of peridotite sample G1-25. (b,c) Transmitted light images of an olivine grain enclosing a group of secondary melt inclusions (Incl). (d) BSE image of a healed crack containing secondary melt inclusions, with the crack showing stronger BSE response (second-generation olivine Ol_2) compared with the host olivine (Ol host). Cpx—clinopyroxene, Gr—garnet, Ol—olivine, Opx—orthopyroxene, Spl—Cr-spinel.

The sample is well-equilibrated, as grains of the rock-forming minerals have uniform major-element composition and show no zoning. The olivine is forsteritic with $Mg\#$ ($100 \times (Mg + Fe)/Mg$) of 92.1 and NiO content of 0.40 wt%, matching the olivine compositions from the previously well-studied V. Grib peridotite suite [93]. The orthopyroxene is enstatite with $Mg\#$ of 92.8; the contents of Al_2O_3 (0.7 wt%), Cr_2O_3 (0.3 wt%) and CaO (0.2 wt%) (Table 1) are also within the range of those for the V. Grib granular peridotites [93,105]. The garnet is pyrope ($Alm_{18}Pyr_{68}Gross_{14}$) with moderate Cr_2O_3 (4.4 wt%) and relatively high CaO (5.4 wt%) amounts, which correspond to the lherzolitic garnet composition according to the classification schemes proposed in [106,107]; the concentra-

tion of TiO₂ (0.12 wt%) is within the range of those for garnet from the V. Grib granular peridotites [93,105]. The clinopyroxene is chromium diopside, showing Mg# of 93.0, Cr₂O₃ of 2.2 wt% and CaO of 20.6 wt%.

Based on olivine–orthopyroxene–clinopyroxene proportions [108], peridotite G1-25 should be classified as harzburgite. However, the presence of Cr-diopside and the typical lherzolitic garnet composition, together with the high Mg# of olivine, indicate the formation of clinopyroxene (and probably garnet) in the initially depleted residua [109] under the re-enrichment processes in the lithospheric mantle beneath the V. Grib pipe [25,93]. Therefore, we argue that it is much more appropriate to classify peridotite G1-25 as garnet lherzolite.

The P-T equilibration parameters for sample G1-25 were obtained using combinations of the two-pyroxene thermometer TA₉₈ [102] and the olivine–garnet thermometer OW₇₉ [110] with the orthopyroxene (Al-in-Opx) barometer NG₈₅ [103]. Both combinations yielded similar results, namely 750 °C and 33 kbar, which match the 37 mW/m² paleo-geotherm [111] constructed previously based on the V. Grib peridotite xenoliths [93,105] and Cr-diopside xenocrysts [94]. The estimated P-T values correspond to a depth of 100 km (Table 1).

4. Methods

Double-polished thin sections and epoxy mounts with embedded olivine grains were prepared from sample G1-25 for further analytical investigation. These were ground and polished without any water-containing abrasives or lubricants to avoid dissolution of water-soluble minerals. All analytical works were performed at the Analytical Center for multi-elemental and isotope research, Siberian Branch of the Russian Academy of Sciences, Novosibirsk, Russia.

Optical microscopy was used to examine the petrographic features of the xenolith, as well as to identify melt inclusions, visually determine their phase compositions and take their photographs in transmitted light. These studies were performed with an Olympus BX-51 microscope coupled with an Olympus DP-74 camera and connected to a PC.

Major element compositions of principle minerals of the xenolith were measured with a JEOL JXA-8100 electron probe microanalyzer (Jeol Ltd., Tokyo, Japan) using wavelength-dispersive spectroscopy (WDS). The analytical conditions were a 20 kV accelerating voltage and a 50 nA beam current, with a beam size of 1 μm [112,113]. Natural mineral standards from the in-house IGM SB RAS collection were used for calibration and instrument stability monitoring. Relative standard deviations were within 1.5%. Data were acquired for 10 s on-peak as well as 10 s on either side of the background; ZAF correction was applied. The detection limits were <0.05 wt% for all the elements analyzed, including 0.01 wt% for Cr and Mn, 0.02 wt% for Ti and Na and 0.05 wt% for K.

Daughter minerals within crystallized melt inclusions were investigated using scanning electron microscopy (SEM) coupled with energy-dispersive X-ray spectroscopy (EDS), as well as with Raman spectroscopy. A TESCAN MIRA 3 LMU scanning electron microscope (Tescan Orsay Holding, Brno, Czech Republic) combined with an EDS INCA Energy detector X-max 80 mm² (Oxford Instruments Nanoanalysis, Abingdon, UK) was used to obtain the following data: (1) back-scattered electron (BSE) imaging of the xenolith texture and exposed inclusions; (2) X-ray maps showing distribution of elements within the exposed melt inclusions; and (3) individual analyses of daughter minerals and bulk analyses of the exposed inclusions. The EDS spectra were optimized for quantification using the standard XPP procedure included in the INCA Energy 350 software. Semi-quantitative analyses of daughter minerals were performed at a 10 kV accelerating voltage.

Raman point measurements of individual daughter minerals within both exposed and unexposed olivine-hosted inclusions were taken with a Horiba Jobin Yvon LabRAM HR800 confocal Raman spectrometer (Horiba, Kyoto, Japan) equipped with a 532 nm Nd:YAG laser and an Olympus BX41 microscope. The 100× objective lens with a numerical aperture of 0.9 was used. The instrument was calibrated using the first-order 520.6 cm⁻¹ band of crystalline silicon. The wavenumbers were accurate to ±1 cm⁻¹. The Raman signal was

collected in the spectral interval of 10–4000 cm^{-1} . The Raman spectra identification was carried out using the RRUFF database [114] as well as other spectra reports (detailed in Tables 2 and 3 and in Section 5.3).

Confocal Raman images of 15 unexposed melt inclusions were collected by acquiring 2D arrays of Raman spectra using a WITec alpha300 R Raman microspectrometer (WITec Company, Ulm, Germany) equipped with a 488 nm laser, an optical microscope Carl Zeiss Axioscope with a short-focus 100 \times objective and a movable piezo-table. The spectra were calibrated using neon lamp emission lines at 540.056, 565.657 and 576.442 nm. The mapped areas were 5 \times 5 μm to 20 \times 20 μm in size, depending on the size of individual crystallized melt inclusions. The spectral resolution was 6 cm^{-1} . The step between the points of the spectra being acquired was 250 nm and the integration time of each spectrum was 1 s.

The WITec Project Five 5.3 software was applied to perform the processing and analysis of the Raman maps. The workflow started with the standard recommended procedures—baseline correction and cosmic-ray band removal (“Graph Background Subtraction-Shape” and “Graph Filter—Cosmic Ray Removal” functions). Then, from the array of Raman spectra, spectra that show bands of individual daughter minerals were selected (“Filters” function). At this stage, false-color images of the distribution of phases within the inclusions were obtained, with the “Combination” function having been used to stack these false-color images. Finally, the number of spectra that corresponded to each daughter mineral was counted and the areas of phase distribution were calculated (“Image Histogram and Statistic” function).

The volumes of daughter minerals (V_{mineral}) were derived from the analysis of the Raman maps of 15 individual melt inclusions. Based on these data, the volume fractions of daughter minerals (φ_{mineral}), mass fractions of daughter minerals (ω_{mineral}) and Ca:Na:K atom ratios for the bulk melt inclusions were calculated.

The volume fractions of daughter minerals within inclusions (φ_{mineral}) were calculated as follows:

$$\varphi_{\text{mineral}} = \frac{V_{\text{mineral}}}{\sum_i^n V_i} = \frac{V_{\text{mineral}}}{V_{\text{total}}}, \quad (1)$$

where $\sum_i^n V_i = V_{\text{total}}$ —sum of volumes of all the daughter minerals within the analyzed melt inclusion or the total volume of the inclusion and n —number of daughter minerals within the inclusion.

The mass fractions of daughter minerals within inclusions (ω_{mineral}) were computed as follows:

$$\omega_{\text{mineral}} = \frac{m_{\text{mineral}}}{\sum_i^n m_i} = \frac{m_{\text{mineral}}}{m_{\text{total}}}, \quad (2)$$

where m_{mineral} —mass of daughter mineral, $\sum_i^n m_i = m_{\text{total}}$ —sum of masses of all the daughter minerals within the analyzed melt inclusion or the total mass of the inclusion and n —number of daughter minerals within the inclusion.

The masses of daughter minerals were calculated by multiplying their volumes V_{mineral} by their densities ρ_{mineral} :

$$m_{\text{mineral}} = V_{\text{mineral}} \times \rho_{\text{mineral}}, \quad (3)$$

Substituting this expression into Equation (2) gives:

$$\omega_{\text{mineral}} = \frac{m_{\text{mineral}}}{\sum_i^n m_i} = \frac{V_{\text{mineral}} * \rho_{\text{mineral}}}{\sum_i^n V_i \rho_i}. \quad (4)$$

The mass fractions of Na_2O , K_2O and CaO within an inclusion are equal to the ratio of the mass of oxide in the inclusion ($m_{\text{oxide}(total)}$) to the total mass of the inclusion (m_{total}):

$$\omega_{\text{oxide}} = \frac{m_{\text{oxide}(total)}}{m_{\text{total}}}. \quad (5)$$

The mass of oxide in the inclusion ($m_{oxide(total)}$) is equal to the sum of the masses of this oxide within all the daughter minerals ($\sum_i^n m_{oxide}^{mineral_i}$), with each term being equal to the product of the mass of a mineral ($m_{mineral_i}$) by the mass fraction of oxide in the mineral ($\omega_{oxide}^{mineral_i}$):

$$m_{oxide(total)} = \sum_i^n m_{oxide}^{mineral_i} = \sum_i^n m_{mineral_i} * \omega_{oxide}^{mineral_i}. \quad (6)$$

Combining Equations (3), (4) and (6) gives the following:

$$\omega_{oxide} = \frac{\sum_i^n m_{mineral_i} * \omega_{oxide}^{mineral_i}}{m_{total}} = \sum_i^n \omega_{mineral_i} * \omega_{oxide}^{mineral_i}. \quad (7)$$

The calculated mass fractions of Na₂O, K₂O and CaO were converted to molar (atomic) ratios Ca:Na:K by dividing by the molar masses of these oxides and normalizing to 1 mol of potassium. The densities of minerals ($\rho_{mineral}$) and oxide mass fractions ($\omega_{oxide}^{mineral}$) were taken from the website <https://www.webmineral.com/> (accessed on 8 March 2023). The Raman spectra of nyerereite (Na,K)₂Ca(CO₃)₂ and shortite Na₂Ca₂(CO₃)₃ are poorly distinguishable during mapping; therefore, it was assumed in the calculations that any of these carbonates were shortite.

To simulate diffusion processes, the Wolfram Mathematics 13 software was employed and we used the finite difference method for solving differential diffusion equations.

5. Results

5.1. Morphology of the Crystallized Melt Inclusions (CMIs)

In xenolith G1-25, grains of rock-forming minerals are populated by a significant number of inclusions. Here, we will discuss only the inclusions enclosed by olivine, since this mineral has a very simple chemical composition (Mg,Fe)₂(SiO₄) and does not concentrate high amounts of trace elements. Thus, reactions between olivine and melt during the formation of secondary melt inclusions can result only in enrichment of the latter in MgO and SiO₂, but not so much FeO, whereas the proportions of all other elements in these inclusions should remain almost unchanged compared to the original melt chemistry.

Figure 2b–d show that the CMIs are typically arranged in groups within randomly oriented healed fractures. The differences in BSE intensity between the host olivine and the olivine that heals the cracks mark these cracks on the mineral surface (Figure 2d). In general, within the error of SEM analysis, the compositions of the host olivine and olivine from healed cracks differ only in FeO content, 7.8 ± 0.05 wt% and 8.0 ± 0.05 wt%, respectively.

The CMIs in olivine vary in size (up to 50 µm) and occur in a variety of shapes, e.g., sub-hedral, round, elongate, irregular and vermicular. Large inclusions are usually elongated or vermicular with rounded edges, whereas small inclusions (up to 10 µm) are rounded or oval, with partially faceted and isometric shapes occasionally being present (Figure 2c). Inclusions that are shaped like negative olivine crystals have not been established.

The CMIs are composed of a series of daughter minerals, whose number within an individual inclusion can reach ten varieties, and a gas bubble (bubbles). In most cases, the daughter phases are transparent and colorless, with most of them showing high birefringence. Opaque mineral grains are present in most inclusions; however, these occupy a significantly smaller volume.

5.2. Mineral Composition of the CMIs

Among the studied mineral assemblage of the CMIs, nineteen phases are considered to be primary magmatic daughter minerals, whereas three (serpentine, magnetite and brucite) are interpreted as secondary post-magmatic minerals of hydrothermal origin (Table 2). The detailed inferences concerning the origin of minerals within the CMIs are provided in the Discussion section.

Table 2. Mineral assemblage of the olivine-hosted melt inclusions in G1-25 garnet lherzolite.

Mineral	Formula	Symbol	SEM-EDS	Raman
Primary magmatic minerals				
Carbonates				
Nyerereite *	(Na,K) ₂ Ca(CO ₃) ₂	Nye	+	+
Shortite	Na ₂ Ca ₂ (CO ₃) ₃	Sot	+	+
Gregoryite/Natrite	(Na,K,Ca) ₂ CO ₃	Gge	+	+
Eitelite	Na ₂ Mg(CO ₃) ₂	Eit	+	+
Bradleyite	Na ₃ Mg(PO ₄)(CO ₃)	Bd	+	+
Northupite	Na ₃ Mg(CO ₃) ₂ Cl	Nup		+
Burkeite	Na ₆ CO ₃ (SO ₄) ₂	Bke		+
Dolomite	CaMg(CO ₃) ₂	Dol	+	+
Calcite	CaCO ₃	Cal	+	+
Magnesite	MgCO ₃	Mgs	+	+
Ba-carbonate		Ba-carb	+	
Sulphates				
Aphthitalite	K ₃ Na(SO ₄) ₂	Att	+	+
Arcanite	K ₂ SO ₄	Acn		+
Phosphates				
Apatite	Ca ₅ (PO ₄) ₃ (F,Cl,OH)	Ap	+	+
Chlorides				
Sylvite	KCl	Syl	+	
Halite	NaCl	Hal	+	
Oxides				
Fe-Ti-Mg Spinel	(Fe,Mg)(Fe,Al,Ti) ₂ O ₄	Fe-Ti-Mg-Spl	+	+
Silicates				
Tetraferriphlogopite	KMg ₃ FeSi ₃ O ₁₀ (OH) ₂	Tfphl	+	+
Sulfides				
Fe-Ni-Cu Sulfide **		Fe-Ni-Cu-Sulf	+	
Secondary post-magmatic (hydrothermal alteration) minerals				
Serpentine	Mg ₃ (Si ₂ O ₅)(OH) ₄	Srp	+	+
Magnetite	FeFe ₂ O ₄	Mgt	+	
Brucite	Mg(OH) ₂	Brc		+

* We use the name “nyerereite” (mineral of orthorhombic symmetry, space group Cmc₂m and composition Na_{1.64}K_{0.36}Ca(CO₃)₂ [115]) for all the carbonates within the melt inclusions with a predominance of Na over K in the A₂ cationic position. However, we have discovered wide variations in the cationic composition of these carbonates and deviations from the classical formula. Even potassium-poor nyerereite with K content of only 0.1 formula units was found (see also Table 3). The Raman spectrum of the potassium-poor nyerereite differs from that of the classical nyerereite and is similar to the Raman spectrum of pure Na₂Ca(CO₃)₂ [116]. ** Nickel-rich iron sulfide was found within inclusions, with minor copper amounts being present in some crystals of this sulfide; however, the grain size and matrix effects did not allow identifying the mineral species. SEM-EDS—the mineral was identified using Scanning Electron Microscopy with Energy Dispersive Spectroscopy. Raman—the mineral was identified using Raman spectroscopy. Mineral symbols (abbreviations) for mineral species are given in accordance with IMA–CNMNC recommendations [117].

Raman spectroscopic and SEM–EDS studies demonstrate that the daughter minerals are represented by Na–K–Ca-, Na–Ca-, Na–Mg-, Ca–Mg-, Ca- and Mg-carbonates, Na–Mg- and Na-carbonates with additional anions, K–Na- and K-sulphates, Na- and K-halides, phosphates, oxides, silicates and sulfides (Table 2, Figures 3 and 4). The following mineral species have been established: nyerereite, shortite, gregoryite/natrite, eitelite, dolomite, calcite, magnesite, unidentified Ba-carbonate, bradleyite, northupite, burkeite, aphthitalite, arcanite, halite, sylvite, apatite, spinel-group minerals, tetraferriphlogopite and unidentified Fe–Ni–Cu-sulfide. All the minerals with crystal–chemical formulas are listed in Table 2.

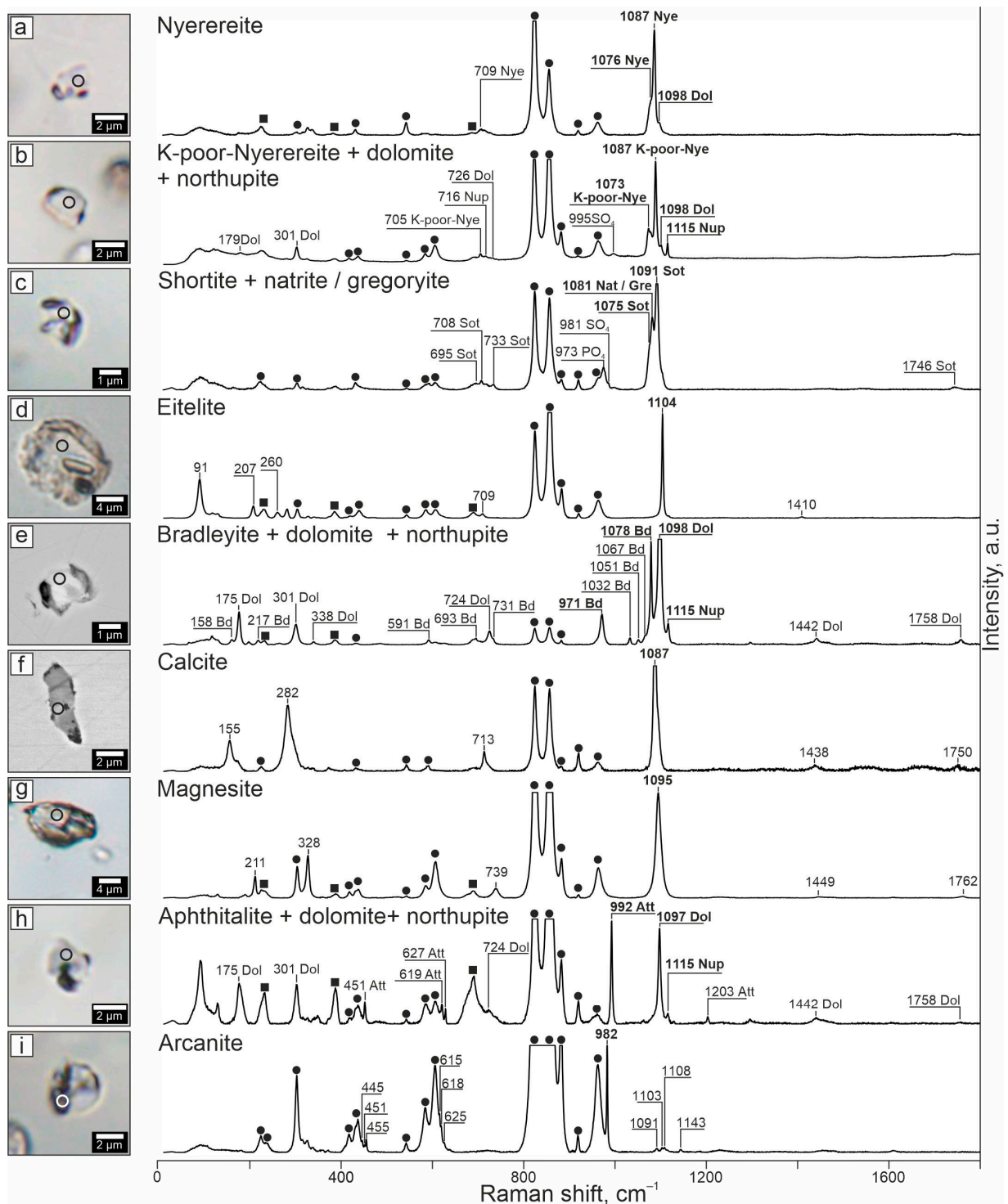


Figure 3. Raman spectra of some daughter minerals within the olivine-hosted secondary melt inclusions from sample G1-25. (a–d,g–i) Transmitted-light images of unexposed inclusions. (e,f) BSE images of exposed inclusions. The circles in the images indicate the spots where the spectra were acquired. The black filled circles in the Raman spectra indicate olivine bands and the black filled squares indicate serpentine bands. Mineral symbols are those defined in Table 2.

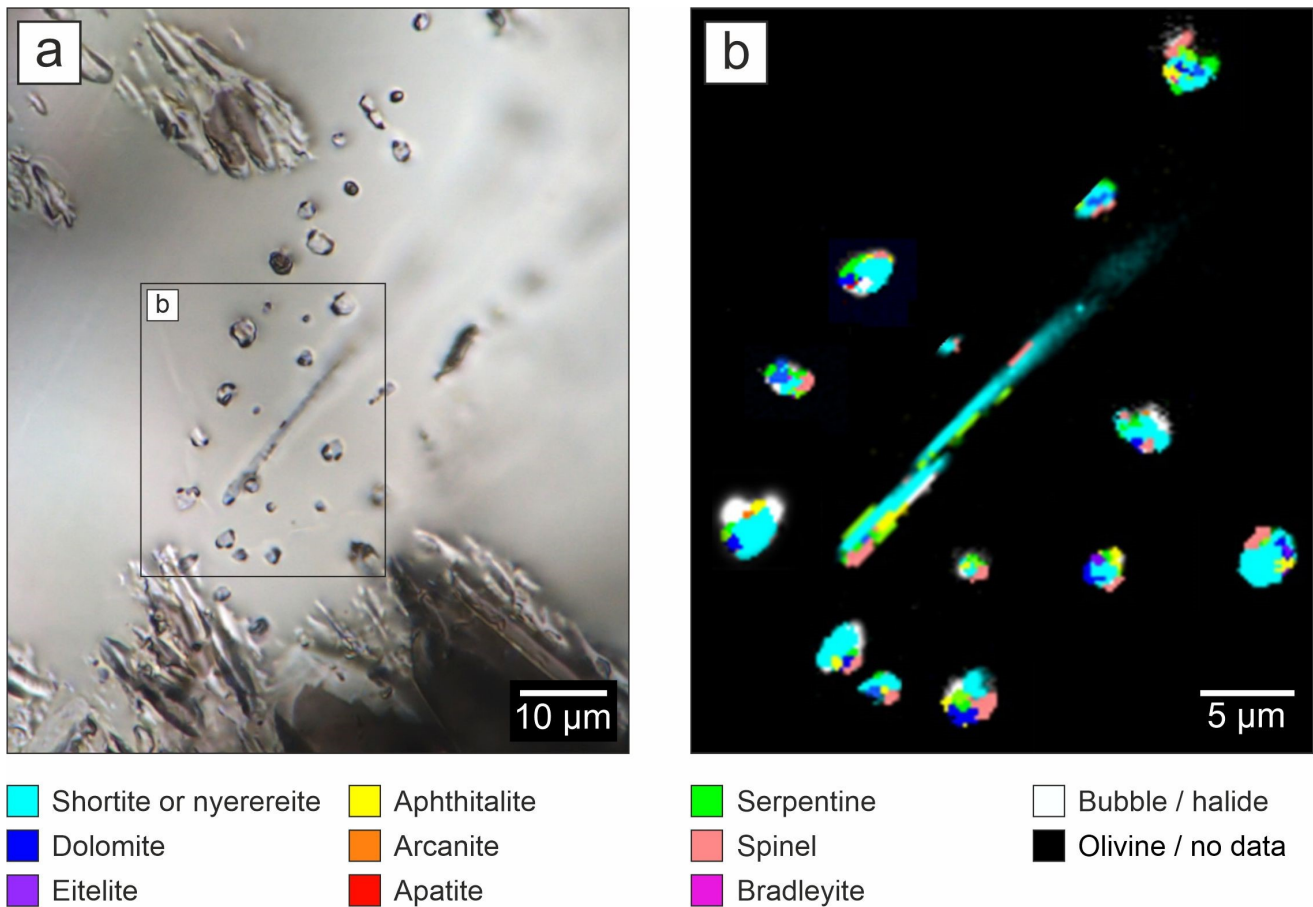


Figure 4. (a) Transmitted-light photomicrograph of secondary melt inclusions in olivine along a healed crack (sample G1-25). (b) Raman map of this group of melt inclusions. Individual minerals are indicated by different colors. The spectral resolution did not allow us to distinguish between Na-Ca carbonates, so both nyerereite and shortite are shown in sky blue. White color denotes areas where the intensity of olivine bands was much less than the intensity of the background, yet no other mineral bands were detected (these regions likely correspond to Raman-inactive chlorides). Those areas where only olivine was detected or that were not studied at all are shown in black.

5.3. Raman Spectroscopic Study of Individual Minerals within the CMI

Nyerereite, a mineral with the empirical formula $(\text{Na}_{1.64}\text{K}_{0.36})\text{Ca}(\text{CO}_3)_2$ [115], was identified by a strong band at $1086\text{--}1087\text{ cm}^{-1}$ with a weak shoulder at $1075\text{--}1076\text{ cm}^{-1}$ in its Raman spectra. The Raman spectra of nyerereite also display a weak band at 709 cm^{-1} (Figure 3a, Table 3, [116,118]). Potassium-poor nyerereite, which is more abundant within the melt inclusions than typical nyerereite, displays Raman spectra that are similar to the spectra of the typical nyerereite [116,119]. These are characterized by a major band at $1086\text{--}1087\text{ cm}^{-1}$, the same as for the typical nyerereite, yet show a distinct medium band at $1072\text{--}1073\text{ cm}^{-1}$ instead of the weak shoulder at $1075\text{--}1076\text{ cm}^{-1}$. The weak band at 705 cm^{-1} is also present in the spectra of the potassium-poor nyerereite (Figure 3b, Table 3, [116,118]).

Another alkaline carbonate, shortite, $(\text{Na,K})_2\text{Ca}_2(\text{CO}_3)_3$, exhibits Raman spectra with two major bands at $1072\text{--}1073$ and $1090\text{--}1093\text{ cm}^{-1}$ and a series of medium/weak bands at $695, 708, 733$ and 1746 cm^{-1} (Figure 3c, Table 3, RRUFF database R040184, [120]). Generally, there are additional Raman bands at $970\text{--}975$ and $980\text{--}1000\text{ cm}^{-1}$, which reflect the vibrations of the PO_4^{2-} and SO_4^{2-} anionic groups (Figure 3c). These Raman bands indicate possible contributions from microinclusions of phosphates (e.g., bradleyite or apatite) and sulphates (e.g., aphthitalite or arcanite) within shortite and/or the presence of the PO_4^{2-} and SO_4^{2-} anionic groups substituting $[\text{CO}_3]^{3-}$ in shortite.

Natrite or gregoryite, Na_2CO_3 , was identified by a distinct band at $1079\text{--}1080\text{ cm}^{-1}$ in the Raman spectra (Figure 3c, Table 3, [116,121]).

The Raman spectrum of eitelite, $\text{Na}_2\text{Mg}(\text{CO}_3)_2$, features an intense band at $1103\text{--}1105\text{ cm}^{-1}$, a medium band at $89\text{--}91\text{ cm}^{-1}$ and three weak bands at 207, 260 and 709 cm^{-1} (Figure 3d, Table 3, RRUFF database R110214, [122,123]).

Dolomite, $\text{CaMg}(\text{CO}_3)_2$, was diagnosed by a strong band at $1097\text{--}1098\text{ cm}^{-1}$, two medium bands at 175 and 301 cm^{-1} and four weak bands at 338, 724, 1442 and 1758 cm^{-1} (Figure 3b,e,h, Table 3, [124,125]).

Bradleyite, $\text{Na}_3\text{Mg}(\text{PO}_4)(\text{CO}_3)$, was identified by two strong Raman bands at 971 and 1078 cm^{-1} . In some instances, the Raman spectra of this mineral also displayed a series of less intensive bands at 158, 217, 591, 693, 1032, 1051 and 1067 cm^{-1} (Figure 3e, Table 3, [126,127]).

The Raman spectra of northupite, $\text{Na}_3\text{Mg}(\text{CO}_3)_2\text{Cl}$, exhibit a strong band at 1115 cm^{-1} and sometimes a less prominent band at 716 cm^{-1} (Figure 3b,e,h, Table 3, RRUFF database R060156, [128]).

Burkeite, $\text{Na}_6(\text{CO}_3)(\text{SO}_4)_2$, was identified by two distinct Raman bands at 995 and 1065 cm^{-1} (Table 3, RRUFF database R060112, [129,130]).

The Raman spectra of calcite, CaCO_3 , are characterized by the following Raman bands: a strong one at 1087 cm^{-1} , two medium ones at 155, 282 cm^{-1} and three weak ones at 713, 1438 and 1750 cm^{-1} (Figure 3f, Table 3, [121,124,125]).

Magnesite, MgCO_3 , is identified by one intense band at 1095 cm^{-1} , two medium bands at 211 and 328 cm^{-1} and three weak bands at 739, 1449 and 1762 cm^{-1} (Figure 3g, Table 3, [121,125]).

The alkaline sulfate apthitalite, $\text{K}_3\text{Na}(\text{SO}_4)_2$, was established by a major Raman band at 992 cm^{-1} and a medium band at 451 cm^{-1} . In addition, there are three bands of low intensity at 619, 627 and 1203 cm^{-1} (Figure 3h, Table 3, RRUFF database R050651, [130]).

Another potassium sulfate, arkanite, K_2SO_4 , shows Raman spectra in which the following bands are present: a strong band at 982 cm^{-1} and several less intensive ones at 445, 451, 455, 615, 618, 625, 1091, 1103, 1108 and 1143 cm^{-1} (Figure 3i, Table 3, [130,131]).

Apatite, $\text{Ca}_5(\text{PO}_4)_3(\text{F,Cl,OH})$, was identified by a strong Raman band at 961 cm^{-1} (Table 3, [132]).

The Raman spectra of Fe-Ti-Mg spinel-group mineral and magnetite, $(\text{Fe,Mg})(\text{Fe,Al,Ti})_2\text{O}_4/\text{FeFe}_2\text{O}_4$, are characterized by a wide band with the center at $665\text{--}685\text{ cm}^{-1}$ (Table 3, [133]).

Tetraferriphlogopite, $\text{KMg}_3\text{FeSi}_3\text{O}_{10}(\text{OH})_2$, displays Raman bands of moderate intensity at 92, 182, 679 and 3706 cm^{-1} (Table 3, [134]).

The Raman spectra of serpentine show the following bands: a pronounced band at $3687\text{--}3698\text{ cm}^{-1}$ (occasionally with a shoulder at $3702\text{--}3704\text{ cm}^{-1}$), with this band resulting from the oscillation of OH groups; three medium bands, whose positions are quite variable even within an individual inclusion and correspond to 229–233, 383–389 and $687\text{--}692\text{ cm}^{-1}$; and a rare weak band at $349\text{--}352\text{ cm}^{-1}$. Such variations in the positions and presence of the bands are likely due to mixtures of chrysotile and lizardite. The Raman bands characteristic of antigorite (strong bands at 3665 cm^{-1} , bands of medium intensity at 374 cm^{-1} and 683 cm^{-1} and weak bands at 638 cm^{-1} and 1045 cm^{-1}) have not been established (Table 3, [135]).

Brucite, $\text{Mg}(\text{OH})_2$, was identified by a strong Raman band at 3641 cm^{-1} with two weak ones at 288 and 448 cm^{-1} (Table 3, [136]).

Table 3. Raman band wavenumbers (cm^{-1}) of the identified minerals within the olivine-hosted melt inclusions in garnet lherzolite (sample G1-25).

Mineral	Raman Region (cm^{-1})				Reference
	0–600	601–900	901–1200	1201–4000	
Olivine (host)	224w, 304m, 316w, 327w, 371w, 431m, 543w, 588m	608m, 824s , 877s , 883w	920m, 964m		
Nyerereite		709w	1076m, 1087s		[116,118]
K-poor-nyerereite		705w	1073m, 1087s		[116,119]
Shortite		695w, 708w, 733w	1075s, 1091s	1746w	[120], RRUFF database R040184
Gregoryite/Natrite			1081s		[116,121]
Eitelite	91m, 207w, 260w	709w	1104s	1410w	[122,123], RRUFF database R110214
Bradleyite	158w, 217w, 591w	693w, 731w	971s , 1032w, 1051w, 1067w, 1078s		[126,127]
Northupite		716w	1115s		[128], RRUFF database R060156
Dolomite	175m, 301m, 338w	724w	1098s	1442w, 1758w	[124,125]
Burkeite			995s , 1065m		[129,130], RRUFF database R060112
Calcite	155m, 282m	713w	1087s	1438w, 1750w	[121,124,125]
Magnesite	211w, 328m	739w	1095s	1449w, 1762w	[121,125]
Aphthitalite	451m	619w, 627w	992s	1203m	[130], RRUFF database R050651
Arcanite	445w, 451w, 455w	615w, 618w, 625w	982s , 1091w, 1103w, 1108w, 1143w		[130,131]
Apatite			961s		[132]
Fe-Ti-Mg Spinel		675s			[133]
Tetraferriphlogopite	92m, 182m	679m		3706m	[134]
Serpentine	229m, 349w, 385m	689m		3689s	[135]
Brucite	288w, 448w			3641s	[136]

s = strong intensity, m = medium intensity, w = weak intensity.

5.4. Volume Ratios of Daughter Minerals within the CMIs

Twelve carbonates and carbonates with additional anions, three minerals that contain the SO_4^{2-} anionic group, three Cl^- -rich minerals and two that contain the PO_4^{3-} group were identified in the CMIs. Among the 19 daughter minerals within the CMIs, there are 12 alkaline-containing minerals, which in turn comprise 6 sodium-, 3 potassium- and 3 sodium–potassium-rich mineral species (Table 2, Figures 3–7).

The volume abundances of carbonate, silicate, sulphate and chloride minerals within the CMIs reached 62, 19, 8 and 5 vol.%, respectively (column 1 in Table 4). The volume ratios of individual minerals within the inclusions were calculated as follows. Initially, mineral volumes were estimated according to Raman mapping of 15 unexposed CMIs (Figure 4). However, chlorides are known to be Raman inactive. To estimate the minimum amount of chlorides, BSE images of 23 exposed CMIs were additionally employed (Figures 5–7).

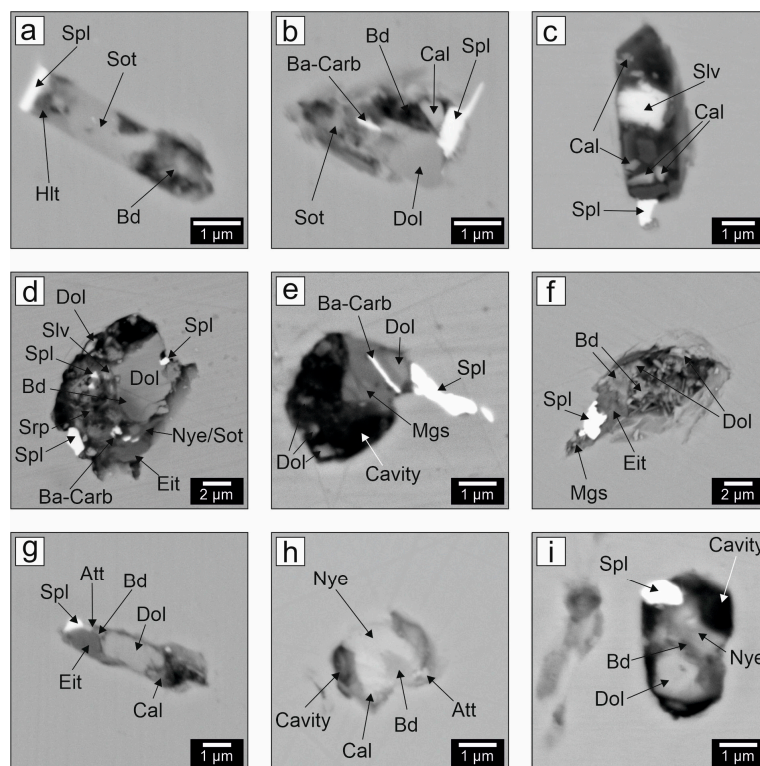


Figure 5. (a–i) BSE images of individual exposed melt inclusions in olivine from xenolith G1-25. X-ray maps showing the distribution of elements within the exposed melt inclusion shown in (d) are presented in Figure 6. Mineral symbols are those defined in Table 2.

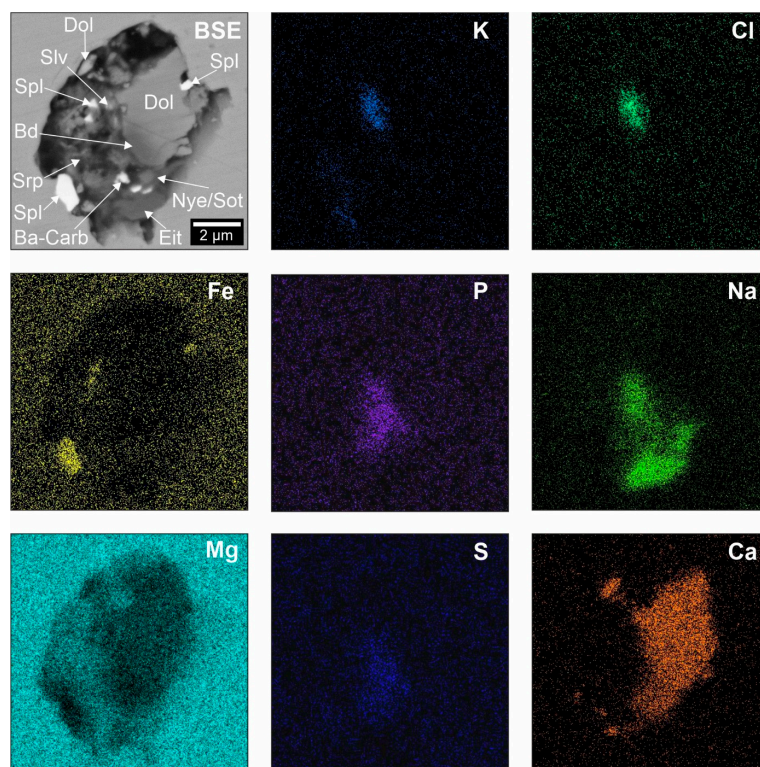


Figure 6. BSE image of an exposed melt inclusion in olivine from sample G1-25 and X-ray maps depicting the distribution of elements within this inclusion. Mineral symbols are those defined in Table 2.

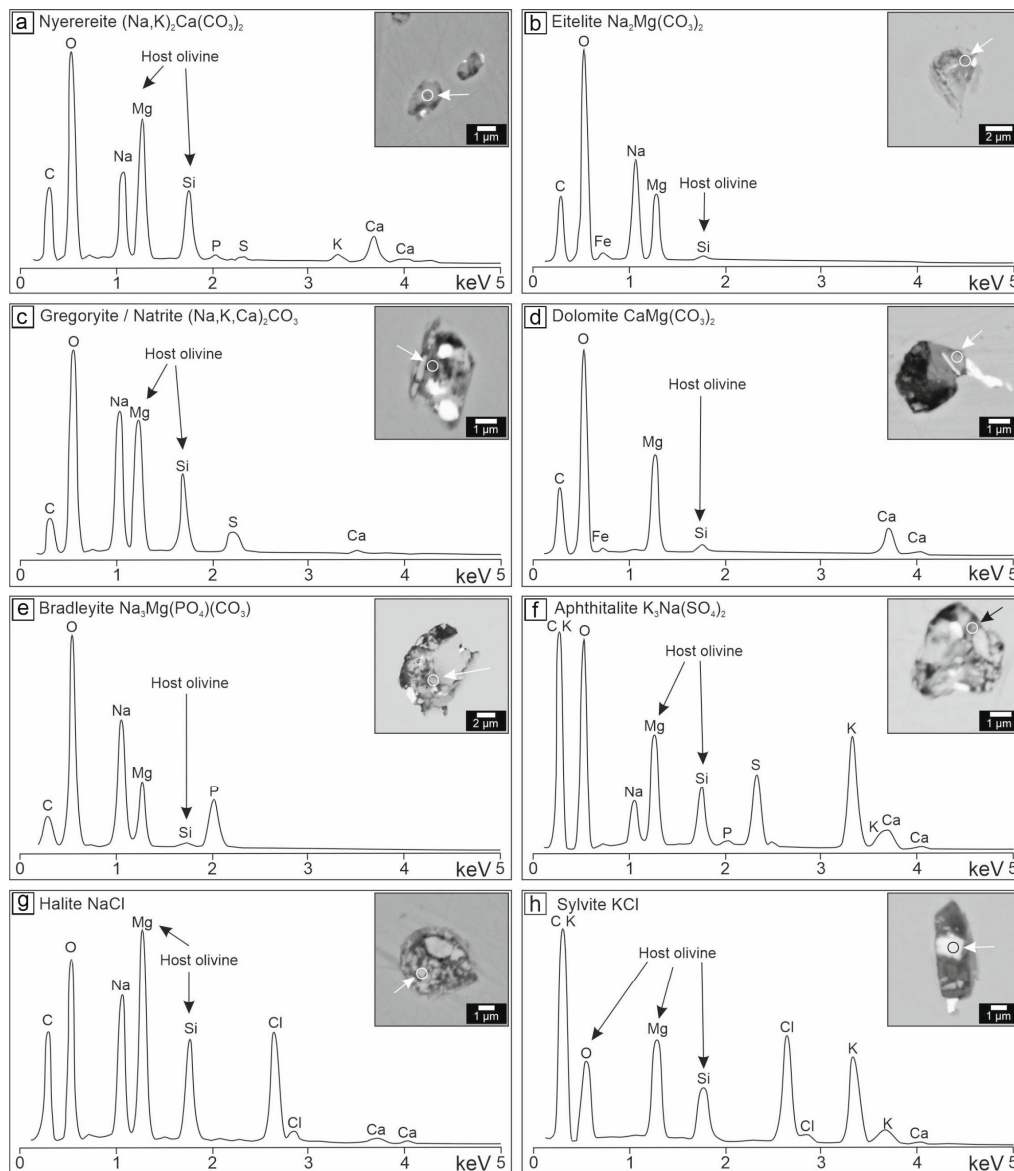


Figure 7. EDS spectra of some daughter minerals (a–h) within the olivine-hosted melt inclusions from xenolith G1-25 coupled with the BSE images of the corresponding inclusions. The arrows and circles in the BSE images indicate the areas where the spectra were collected.

Using (1) Raman mapping data (Figure 4) and (2) SEM bulk analyses of the exposed CMIs (Figures 5–7), the Ca:Na:K atomic ratios for the bulk CMIs were calculated. The former approach yielded a Ca:Na:K ratio of 5.2:2.3:1, whereas the latter method provided a Ca:Na:K ratio of 5.7:4.7:1.

In the first case, the contents of alkalis relative to calcium are significantly underestimated due to the fact that: (i) chlorides do not give Raman spectra and (ii) Raman mapping does not permit distinguishing between shortite and nyerereite, so that calculation of the minimum sodium contents was made using shortite stoichiometry $\text{Na}_2\text{Ca}_2(\text{CO}_3)_3$ rather than that of nyerereite, $(\text{Na,K})_2\text{Ca}(\text{CO}_3)_2$. The second estimate looks more realistic, although the abundances of Na and, to a lesser extent, K are likely underestimated with respect to Ca as well because of possible alkali burnout in the CMIs during SEM bulk analysis and also due to the late serpentinization of the CMIs by aqueous fluids. The origin of serpentine in the CMIs and some implications for the bulk composition of the inclusions in general, and Na levels in particular, are addressed in more detail in the Discussion section.

Table 4. Volume ratios of minerals within the olivine-hosted melt inclusions in garnet lherzolite (sample G1-25).

Mineral	1 *	2	3	4	5
Shortite + nyerereite	46.4%	46.4%	53.1%	49.9%	57.8%
Eitelite	1.3%	1.3%	1.4%	1.4%	1.6%
Dolomite	7.6%	7.6%	8.6%	8.1%	9.4%
Calcite	3.8%	3.8%	4.4%	4.1%	4.8%
Magnesite	0.5%	0.5%	0.6%	0.6%	0.6%
Bradleyite	1.7%	1.7%	2.0%	1.9%	2.2%
Northupite	0.5%	0.5%	0.6%	0.6%	0.6%
Aphthitalite	7.0%	7.0%	8.0%	7.5%	8.7%
Arcanite	0.7%	0.7%	0.8%	0.7%	0.8%
Sylvite	3.2%	3.2%	3.7%	3.5%	4.0%
Halite	2.1%	2.1%	2.5%	2.3%	2.7%
Apatite	0.7%	0.7%	0.8%	0.8%	0.9%
Fe-Ti-Mg Spinel	3.1%	2.4%	2.8%	2.6%	3.0%
Tetraferriphlogopite	2.3%	2.3%	2.6%	2.5%	2.8%
Serpentine	16.7%	0.0%	0.0%	0.0%	0.0%
Brucite	2.3%	0.0%	0.0%	0.0%	0.0%
Olivine	0.0%	12.6%	0.0%	13.6%	0.0%
H ₂ O **	0.0%	7.1%	8.2%	0.0%	0.0%
Total	100.0%	100.0%	100.0%	100.0%	100.0%
Carbonates ***	61.8%	66.5%	77.0%	66.5%	77.0%
Sulphates ***	7.7%	8.2%	9.5%	8.2%	9.5%
Chlorides ***	5.3%	5.8%	6.7%	5.7%	6.7%

*—The values (Raman mapping data) were averaged over 15 unexposed inclusions from 1 group. BSE images combined with X-ray maps of 23 exposed melt inclusions were used to estimate the minimum amount of Raman-inactive chlorides. ** For modeling and calculating, it was taken into account that water is liquid and its density is 1 g/cm³. With a decrease in the density of water, the volume of the fluid phase in the inclusions may increase. *** The volume percentage of chlorides, sulfates and carbonates among solid phases (excluding liquids and gases). The initial phase composition of the inclusions can be constrained by the following estimates: 1. actual ratios of minerals within the inclusions including post-magmatic (hydrothermal alteration) serpentine + brucite; 2–5—calculated initial phase composition of the inclusions based on the following models: 2. serpentine is formed by the reaction of daughter olivine with deuterium/magmatic water; 3. serpentine is formed by the reaction of olivine matrix with deuterium/magmatic water; 4. serpentine is formed by the reaction of daughter olivine with external water; 5. serpentine is formed by the reaction of olivine matrix with external water.

The widespread abundance of Na-, K-, CO₃²⁻, SO₄²⁻, PO₄³⁻ and Cl⁻-rich phases in the CMIs implies high concentrations of these elements in the parental melt. Therefore, the examined daughter mineral assemblage within the CMIs indicate that the melt parental to these inclusions was a carbonate liquid, probably of alkaline specifics (rather than calcium), with a high content of volatiles such as S, P, Cl and low amounts of SiO₂ (≤9.6 wt%) and H₂O (≤2.6 wt%).

6. Discussion

6.1. General Models for the Origin of Secondary Melt Inclusions in Minerals of Mantle Xenoliths

According to the data given in [86], secondary melt inclusions in minerals of mantle xenoliths from numerous worldwide occurrences of basaltoids (mafic rocks) have been studied for over 50 years. As yet, however, melt inclusion research of mantle xenoliths from kimberlites (ultramafic igneous rocks) is at an early stage of its development (see review in [20]).

More than ten scenarios have been proposed for the origin of secondary melt inclusions in mantle xenoliths from mafic igneous rocks. The principle models are: (i) mantle metasomatism scenario, i.e., infiltration of migrating melts/fluids into mantle rocks, which takes place long before the entrapment of xenoliths by ascending magma; this model does not imply any genetic relationship between the formation of inclusions and magmatism that finally formed basaltoid bodies at the surface; (ii) partial melting of primary minerals of mantle rocks; this model involves decomposition of water-containing xenolith phases at

heating or decompression or during reactions with migrating melts; and (iii) interaction of xenoliths with transporting melts during xenolith ascent to the surface. According to reviews in [85–88], the first scenario is the most popular, whilst the last one is the least accepted.

Until now, secondary melt inclusions in olivine of mantle xenoliths from kimberlites have been studied only in a certain structural type of rocks—so-called sheared peridotites. These peridotites, in contrast to the coarse-grained ones, exhibit a porphyroclastic texture made up of large porphyroclasts (1–10 mm) of olivine, garnet and pyroxenes that are set in a matrix composed of very fine-grained neoblasts (0.1–0.5 mm) of predominant olivine and subsidiary pyroxene. Some deformation microstructures of sheared peridotites could not be preserved for more than a few years during annealing at the temperatures recorded by their mineral chemistry [137–139]; thereby, it is generally accepted that sheared peridotites are formed shortly before their capture by kimberlitic magma (e.g., [68,140]). In general, as summarized in [140], the deformation of the peridotite rocks in the lower cratonic lithosphere is due to a combination of localized stress, heating and fluid migration through the mantle substrate near the pathways of ascending kimberlite melts. The presence of the same minerals within secondary melt inclusions both in porphyroclasts and neoblasts of olivine indicates that infiltration of melt along fractures occurred after the deformation of the peridotites [68,69].

Therefore, for secondary melt inclusions in olivine from sheared peridotites, only two scenarios of their origin are possible.

The first scenario implies that primitive kimberlite (by composition) or proto-kimberlite (by time) melts/fluids originate from local sources and percolate through the mantle substrate at the pre-eruption stage. Growth of localized stress in the interstitial space of mantle peridotites in the presence of such liquids should lead to cracking of rock-forming olivine in situ and, at the same time, to healing of these cracks by the interstitial melt coupled with the formation of swarms of secondary melt inclusions.

The second scenario involves the infiltration of kimberlite melt into entrapped xenoliths during magma ascent. The model of Brett et al. (2015) [141], which is based on numerical calculations, shows that peridotitic olivine grains start to develop internal cracks after 15–25 km from the entrapment level at the ascent velocities of 0.1 to $>4 \text{ m s}^{-1}$ expected for kimberlite magma. Because carbonatite melt has low viscosity and appropriate wetting properties, its infiltration into cracks within olivine grains and healing of these cracks with the formation of secondary melt inclusions would occur almost simultaneously with olivine cracking.

Hence, when reconstructing the processes of formation of secondary melt inclusions in olivine from sheared peridotites, one or even both of the above scenarios should be taken into account, and both of these scenarios support a genetic link between the formation of this type of inclusions and kimberlite magmatism.

6.2. Nature and Depth of Formation of the CMIs in the Peridotite Xenolith from the V. Grib Kimberlite

Infiltration of melt into entrapped xenoliths during magma ascent is the probable scenario for the origin of secondary melt inclusions in both coarse-grained peridotite xenoliths from basaltoids and sheared peridotites from kimberlites. The other models are generally applicable to either mantle xenoliths from basaltoids or sheared peridotites from kimberlites. For instance, since accessory phlogopite (water-rich phase) is present in the examined coarse-grained peridotite xenolith from the V. Grib pipe, there is no reason to apply to this sample the model of the decomposition of water-bearing xenolith phases, which is sometimes used for basaltoid xenoliths. Moreover, carbonate liquids cannot occur as a result of the partial melting/breakdown of the minerals (mostly silicates) present in this peridotite xenolith.

We will consider the following three scenarios for the formation of the CMIs in the peridotite xenolith from the V. Grib kimberlite pipe. These include: (1) in situ infiltration

of a kimberlite-related liquid into the peridotite shortly prior to the pre-eruption stage, (2) infiltration of the kimberlite melt into the entrapped xenolith during magma ascent and (3) mantle metasomatism scenario that takes place long before the entrapment of the xenolith by ascending magma. The first two scenarios, which relate the origin of the CMIs to the kimberlite magmatism, are, in our opinion, the most preferable. Some considerations supporting the first two models are presented below.

The CMI residence time at the P-T parameters of the lithospheric mantle (750 °C and 3.3 GPa, which corresponds to the last mineral equilibrium of the studied xenolith) cannot be reliably determined. However, the time order of magnitude can be estimated by two independent approaches.

The first approach involves estimation of melt inclusion faceting time. The studied CMIs have different shapes: oval, elongated, vermicular and dendritic. Such shapes of inclusions are characterized by high values of surface free energy. The minimization of surface free energy at high temperatures is a spontaneous process that causes the inclusion to take the form of a host mineral negative crystal [142]. However, such negative crystal shapes have not been identified among the studied inclusions. To the best of our knowledge, no published works have yet addressed the timescales of faceting of olivine-hosted melt inclusions at the lithospheric mantle P-T parameters. Nevertheless, a “geospeedometer” based on faceting of quartz-hosted melt inclusions was proposed [143]. This “geospeedometer” was created based on the study of zoned quartz phenocrysts from Bishop Tuff, California, which crystallized in a magma chamber at the depth range of 4–10 km [144]. It was demonstrated that the faceting time of spherical inclusions can be calculated as follows:

$$\Delta t = \frac{-RT}{8\pi DC_0\sigma\Omega} \Delta V, \quad (8)$$

where C_0 is the solubility of the mineral in the melt, σ is the surface energy, Ω is the molar volume of the host mineral, R is the ideal gas constant, T is temperature, D is the diffusion coefficient and ΔV is the volume of the host mineral that needs to be dissolved and recrystallized in order to transform the spherical inclusion into an inclusion having a negative crystal shape. The ΔV parameter depends on the linear dimensions of the inclusion; therefore, large inclusions require more time to become faceted. Taking Equation (8) into account, calculations show that at 750 °C, a quartz-hosted inclusion of rhyolite melt 10 μm in size would obtain a negative crystal shape in 0.3 years [143]. With a decrease in temperature, the diffusion coefficient decreases rapidly; therefore, at low temperatures, faceting of inclusions is impossible. Hence, faceting time in our case is likely limited by the CMIs residence time at the lithospheric mantle P-T parameters.

The second approach is based on an estimation of the equilibration time between the olivine from healed cracks and the host olivine. Diffusion processes occur where there are concentration gradients and lead to equalization of the concentrations. Numerically, diffusion is characterized by the diffusion coefficient, which is a function of temperature, pressure and system chemistry. A simulation of Fe diffusion between olivine from healed cracks and the host olivine has been performed. The concentration of FeO within the two olivine generations at the initial moment of time was provided to the simulation: within the healed crack, which is 2 μm thick, the FeO concentration was 8.0 wt%, whereas within the host olivine, FeO level was 7.8 wt%. The distribution of Fe within olivine over time was calculated using the Fick equation:

$$\frac{\partial C}{\partial t} = D \frac{\partial^2 C}{\partial x^2}, \quad (9)$$

where C —concentration, t —time, x —coordinate in a direction perpendicular to the plane of the healed crack and D —diffusion coefficient. Here, we employed the experimentally determined at 750 °C and at 3.3 GPa diffusion coefficient $D = 10^{-18.64} \text{ m}^2/\text{s}$ [145]. The simulation did not take into account diffusion along the crack plane (along the y and z axes) since there is no concentration gradient along these directions. The calculations show

that after 4 months the difference between the concentrations of FeO within these two generations of olivine will decrease by a third, and after 10 months the difference will become unnoticeable (Figure 8). Since the formation of melt inclusions and crack healing occur synchronously and diffusion proceeds very slowly at near-surface temperatures, the iron rebalancing time between the olivine within healed cracks and the host olivine (~1 year) can be used to constrain the time order of magnitude for the CMI residence at the P-T parameters of the lithospheric mantle.

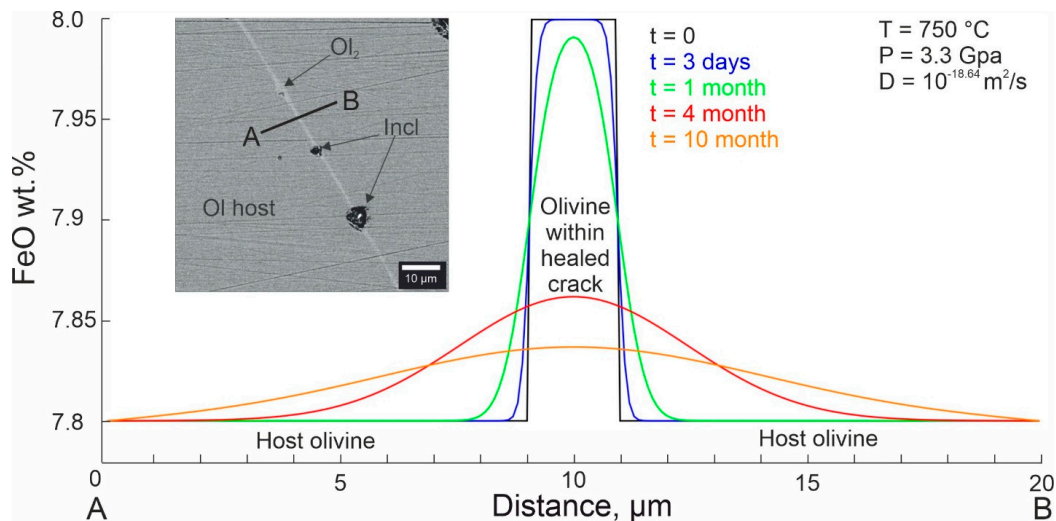


Figure 8. BSE image and FeO concentration profiles of the rock-forming olivine (Ol host, initial $C(\text{FeO}) = 7.8 \text{ wt}\%$) across a healed crack (Ol_2 , initial $C(\text{FeO}) = 8.0 \text{ wt}\%$). The profiles were constructed for the initial moment of time (t) and after 3 days, 1 month, 4 months and 10 months of iron diffusion along the line (A,B) at $T = 750 \text{ }^\circ\text{C}$ and $P = 3.3 \text{ GPa}$. D —diffusion coefficient.

Since the studied CMIs lack negative crystal morphologies (Figure 4) and compositional heterogeneity between the two olivine generations is present (Figure 8), we conclude that the CMIs existed for a very short time span at the P-T parameters of the lithospheric mantle.

Other evidence in favor of the first two hypotheses comes from the mineral and chemical compositions of the CMIs, including the new results presented here. Based on the bulk composition of kimberlite rocks, it is conventionally believed that primary/primitive kimberlitic liquids are of ultramafic composition, with SiO_2 and MgO concentrations (both individually and collectively, $\text{SiO}_2 + \text{MgO} \geq 50 \text{ wt}\%$) dominating over the abundances of other oxides (e.g., [146]) and maximum individual SiO_2 and MgO concentrations reaching as much as 35 wt% (e.g., [66]). However, the direct investigation of preserved kimberlite melts, namely modern melt inclusion studies of kimberlite minerals and mantle xenoliths from kimberlites, provided compelling evidence that at any stage of the life cycle of kimberlite melts, these liquids were alkali-rich and carbonatitic in composition (e.g., [20,67–84]). The carbonatite nature of kimberlite melts is also confirmed by mass balance calculations, evaluations of the volume amounts of xenogenic olivine in kimberlite rocks and dissolution of mantle silicates from disintegrated mantle xenoliths at interaction with kimberlite melts (e.g., [84,147–160]).

We have carried out a comparative analysis of the CMI mineral assemblage in the coarse-grained peridotite investigated here with the daughter minerals of secondary melt inclusions in sheared mantle xenoliths from other kimberlite pipes: Udachnaya–East, Komsomolskaya–Magnitnaya (Siberian craton) and Bultfontein (Kaapvaal craton). The results appear in Table 5.

Table 5. Comparison of the studied mineral assemblage within secondary melt inclusion from V. Grib garnet lherzolite xenolith, with mineral assemblages of secondary melt inclusions in mantle xenoliths from other kimberlite pipes: Udachnaya–East, Komsomolskaya–Magnitnaya and Bultfontein.

Name of Kimberlite Pipe	V. Grib	Udachnaya–East	Komsomolskaya–Magnitnaya	Bultfontein
Craton	Baltic	Siberian	Siberian	Kaapvaal
Age, Ma	376 ± 3 [91]	363–367 [161]	334–402 * [162–164]	81–92 [165,166]
Depth **, km	100 (this study)	179–227 [67–69]	198–208 [70,167]	112–152 [71,72]
Type of xenoliths	Granular	Sheared	Sheared	Sheared
	Mineral assemblage			
	Carbonates			
Nyerereite	•	•	•	•
Shortite	•	•	•	•
Gregoryite/Natrite	•			•
Eitelite	•	•	•	•
Bradleyite	•	•		•
Northupite	•	•		•
Dolomite	•	•	•	•
Burkeite	•	•	•	•
Tychite		•	•	•
Calcite	•	•	• ^{?***}	•
Aragonite		•	• ^{?***}	
Magnesite	•	•	•	•
Ba-carbonate	•			•
	Sulphates			
Aphthitalite	•	•	•	•
Arcanite	•			•
Glauberite				•
Thenardite			•	•
	Phosphates			
Apatite	•	•	•	•
	Sulphides			
Pyrrhotite	• ^{****}	•	•	
Pentlandite	• ^{****}	•		
Djerfisherite		•	•	
Rasvumite		•		
Heazlewoodite				•
	Chlorides			
Sylvite	•	•	•	•
Halite	•	•	•	•
Chloromagnesite		•		
	Oxides			
Rutile		•		•
Perovskite		•		•
Ilmenite		•		•
Chromite		•		
Fe-Ti-Mg Spinel	•	•	•	•
Magnetite	•	•	•	•
	Silicates			
Phlogopite		•	•	•
Tetraferriphlogopite	•	•	•	•
Olivine		•	•	
Diopside		•	•	
Sodalite		•		
Richterite		•		•
Monticellite			•	
Serpentine	•			•
Reference for mineral assemblages	this study	[67–69,123,129,168–170]	[70,167]	[71,72]

* There are no reliable U–Pb data on the age of the Komsomolskaya–Magnitnaya pipe. Estimates of the kimberlite age using the K–Ar method are in the range of 367 to 345 Ma [162,163], whereas Rb–Sr dating of phlogopite megacrysts yielded 400–402 Ma [164]. ** Depth of the last mineral equilibrium. *** Polymorph of CaCO₃ carbonate is not well defined. **** Nickel-rich iron sulfide was found within inclusions, with minor copper amounts being present in some crystals of this sulfide; however, the grain size and matrix effects did not allow identifying the mineral species.

This table shows that, regardless of xenolith structural type, age, or geographic location of kimberlites, the mineral composition of the olivine-hosted CMIs in xenoliths from different kimberlites is nearly identical, and that such an association of daughter minerals within the inclusions corresponds to alkali-rich carbonatite in all cases. This, in our opinion, cannot be a simple coincidence. The only difference in the mineral composition of the inclusions is the presence or absence of secondary post-magmatic water-rich minerals, mainly serpentine, which will be addressed below.

Therefore, we suggest that the olivine-hosted CMIs in the examined peridotite xenolith are genetically related to the magmatism that subsequently formed the V. Grib pipe, with the composition of these inclusions corresponding to that of the kimberlitic liquids at some stage of their evolution. Further study of melt inclusions in the V. Grib kimberlite minerals, as well as of the minerals of sheared peridotite xenoliths from the V. Grib pipe, should unambiguously confirm or refute our conclusions.

Based on the above arguments, the third scenario (“old metasomatic event”) is unlikely, and there are no data confirming it.

In general, according to any of the three models presented, the liquid parental to the examined CMIs percolated into olivine either in situ in the mantle or 15–25 km following the xenolith entrapment during its transportation to the surface, i.e., at a depth of ~100 or ~80 km, respectively. Consequently, this parental liquid should have originated at depths below 100 km.

6.3. The Nature of Post-Magmatic Serpentine and the Influence of Serpentinization on the CMI Original Composition

According to the above models of the CMI formation, there is no doubt that such inclusions are associated with mantle processes, and all of the carbonates, sulfates, chlorides, sulfides, apatite, Fe-Ti-Mg spinel and tetraferriphlogopite in the peridotite xenolith from V. Grib are daughter magmatic minerals.

This conclusion is independently confirmed by the study of inclusions in natural diamonds and experimental studies of various systems. The same suite of daughter minerals (Na-K-Ca-Mg-bearing carbonates, alkali sulfates and chlorides in various combinations) has been identified within inclusions in lithospheric and sublithospheric diamonds (see Introduction). Experimental studies show that in the system $\text{Na}_2\text{CO}_3\text{--CaCO}_3\text{--MgCO}_3$ at 3 GPa and 700–950 °C, liquidus minerals are nyerereite, shortite, eitelite and dolomite. The same system at 3 GPa up to 1285 °C has primary solidification phase regions for magnesite, dolomite-calcite solid solutions, calcite and Na carbonate [171]. In the products of melt quenching synthesized at 5 GPa and 1500 °C in the $\text{CaMgSi}_2\text{O}_6\text{--Na}_2\text{CO}_3(\pm\text{CaCO}_3)\text{--KCl}$ model system, shortite (or nyerereite) was identified as well [172].

Thus, only three interrelated issues remain unresolved: (1) the origin of serpentine in the CMIs, (2) the influence of serpentinization processes on the CMIs mineral composition and (3) the composition of the CMIs’ parental melt if the postmagmatic serpentinization is taken into account.

It is accepted that serpentine is not stable at mantle temperatures above 700 °C (Figure 9a). Therefore, this mineral could not occur within the studied rock in situ in the mantle section. Moreover, no antigorite, i.e., a relatively high-temperature serpentine polymorph stable up to 690 °C (Figure 9a, [173,174]), was established in the CMIs. The Raman data imply that serpentine inside the CMIs is represented by a mixture of lizardite and chrysotile, with the former predominating. Thermodynamic calculations, laboratory studies and field observations show that lizardite originates in the temperature range of 50–300 °C and is common in low-temperature hydrated olivine-bearing rocks (Figure 9b, [175]). Such low temperatures of serpentine formation in the inclusions (≤ 300 °C) do not correspond to any magmatic process, and thus serpentine in the inclusions can only be a postmagmatic hydrothermal mineral.

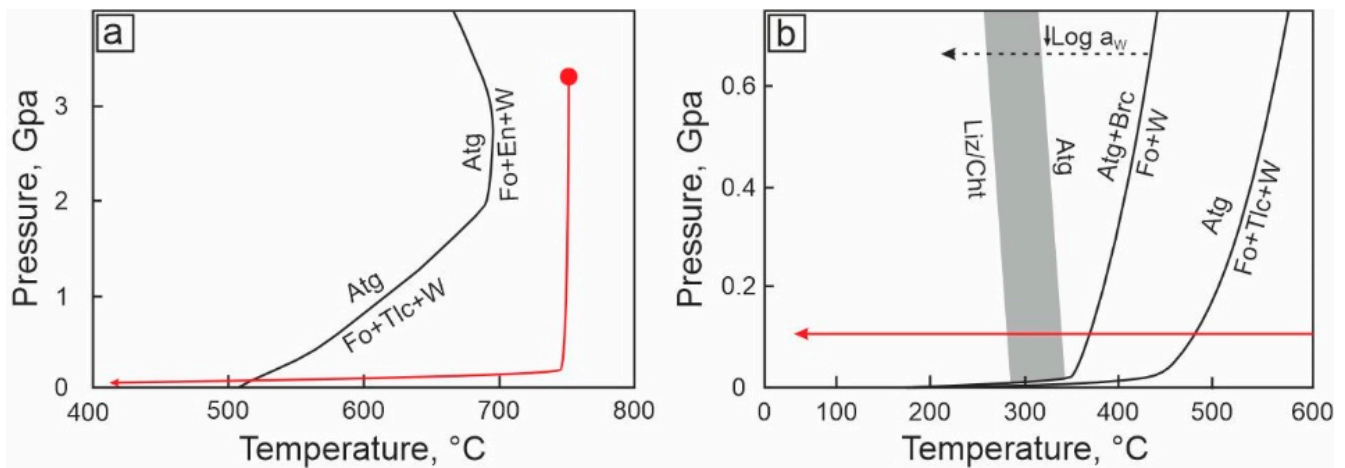


Figure 9. Serpentine stability region in the P-T stable phase diagram for the system MgO-SiO₂-H₂O with the P-T trend evolution of xenolith G1-25 during ascent and post-magmatic cooling (red line). The P-T parameters of the last mineral equilibrium of the xenolith are marked by the red filled circle. (a) High-temperature part of the P-T diagram. Two reactions of serpentine decomposition are shown by the solid black line [173,174]. (b) Low-temperature and low-pressure area of the P-T diagram. The solid black lines show olivine hydration reactions. The gray field separates antigorite formation- and lizardite/chrysotile-formation areas. The dotted line shows that as water activity ($\log a_w$) decreases, reaction temperature decreases as well. The P-T diagram is from [175]. Liz—lizardite, Cht—chrysotile, Brc—brucite, Atg—antigorite, Fo—forsterite, Tlc—talc, W—water, En—enstatite.

It is apparent that the serpentinization of mantle xenoliths (Figure 10) is directly related to the serpentinization of their host kimberlites at near-surface conditions. We posit that the serpentinization of the inclusions is closely linked to the serpentinization of the xenolith (Figure 10) by external aqueous solutions. This assumption is strongly supported by the fact that mantle peridotite xenoliths and megacrysts (e.g., [8–10,17,19,26,140,160,176,177]) from non-serpentinized kimberlite varieties of the Udachnaya–East pipe [79,147,148,178–182] show absolutely no evidence of serpentinization, whereas in partially serpentinized kimberlites of the Udachnaya–East pipe, the xenoliths contain serpentine (e.g., [183]).

The long-term melt inclusion studies of non-serpentinized peridotite xenoliths from Udachnaya–East (about 1000 Raman and SEM analyses) established that no serpentine is present among the daughter minerals in olivine-hosted secondary CMIs from these xenoliths (Table 5, column 3; [67–69]). It is worth noting that the serpentinization does not occur as a continuous front in transitional varieties of serpentinized to non-serpentinized kimberlites of the Udachnaya–East pipe, but rather develops unevenly in the form of elongated bands and localized spots.

Another argument supporting an external source of water during the serpentinization stems from the uneven distribution of serpentine inside the studied CMIs. It is of importance that many individual inclusions lack serpentine (Figure 5). Even within a local swarm of inclusions, the content of serpentine in individual CMIs varies from 0 to 27 vol.% (Figure 4).

At the moment, we cannot build an unambiguous model of how postmagmatic hydrothermal serpentine is formed in individual secondary CMIs in olivine of partially serpentinized xenoliths. It is possible that the penetration of external aqueous solutions into CMIs is facilitated by the presence of optically invisible microcracks or channels in olivine. A series of experiments on the serpentinization of peridotites may help to solve this problem.

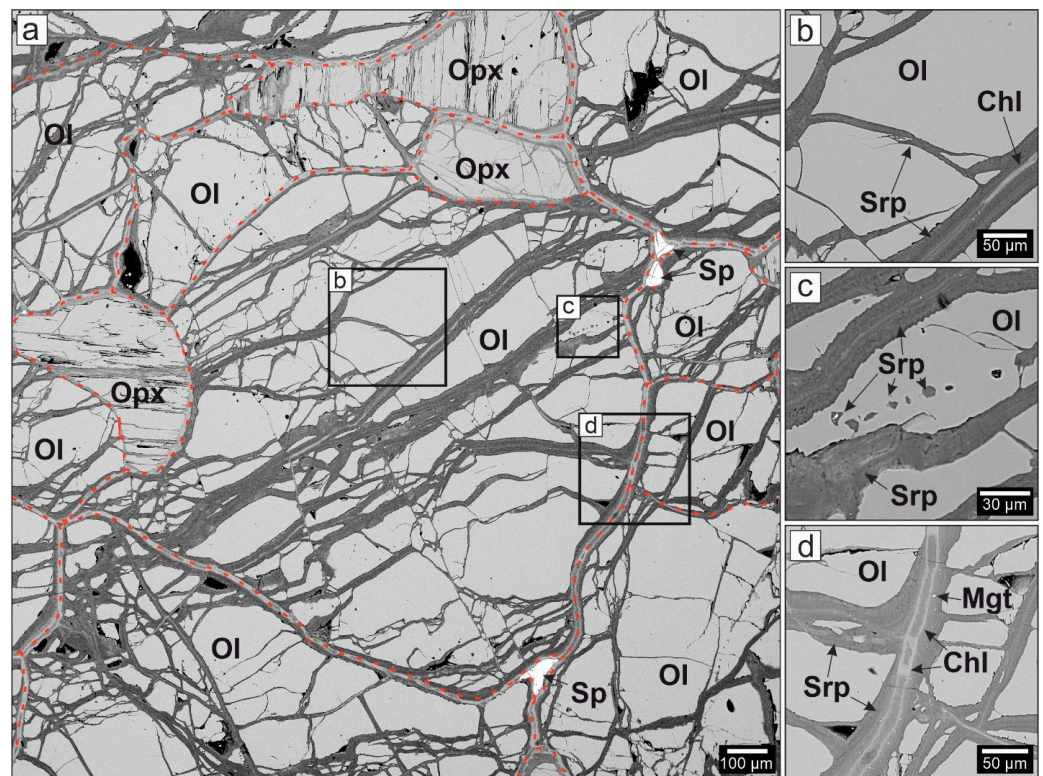


Figure 10. BSE images depicting serpentine and serpentine–chlorite aggregates in xenolith G1-25. (a) Xenolith texture. Grains of rock-forming olivine, orthopyroxene and spinel are shown, with the boundaries between them marked by the red dotted lines. Serpentine was found around grains of the rock-forming minerals and in veins crosscutting olivine and orthopyroxene. (b) Serpentine in veins crosscutting olivine grains. Large veins are zoned: ferruginous chlorite is contained in the central part, and serpentine is confined to the marginal parts of the veins. Small veins are filled only by serpentine. Some small serpentine veins are associated with empty cracks. (c) Serpentine veins and a group of altered secondary melt inclusions (replaced by serpentine) in olivine, with a crack connecting the serpentine vein with one of the inclusions. (d) Boundary between rock-forming olivine grains. A zoned serpentine–chlorite aggregate associated with magnetite crystals is present in the interstitial space. Ol—olivine, Opx—orthopyroxene, Sp—spinel, Srp—serpentine, Chl—chlorite, Mgt—magnetite.

It would also be premature to state that the source of water for the entire serpentine within the inclusions is of external, non-magmatic origin, at least because of the possible high water solubility in carbonatite melts. For instance, according to experimental data [184], water solubility in Ca-Na-Mg carbonate melt at 900 °C already at 1 kbar can reach nearly 10 wt%. For the same system $\text{CaCO}_3\text{--Na}_2\text{CO}_3\text{--MgCO}_3$ at 1 bar, however, the water solubility drops to ~0.5 wt% H_2O at 900 °C [185]. Nonetheless, the total weight of water in inclusions calculated from the volume of a water-rich association lizardite (1.9 wt% H_2O) + brucite (0.6 wt% H_2O) + tetraferriphlogopite (0.1 wt% H_2O) is 2.6 wt% (Table 4). Thus, according to [185], under surface conditions, inclusions could contain ~2 wt% H_2O in the form of a free fluid phase. The model temperatures of kimberlite magma at near-surface conditions are ~1100–1200 °C [186], whereas the equilibrium temperature of the studied xenolith is 750 °C (Table 1), implying that the xenolith temperature at near-surface conditions during eruption could not be lower than 750 °C. According to [173–175] (Figure 9), the temperature drop in the xenolith during the formation of a kimberlite body, given the presence of a free aqueous phase in the olivine-hosted inclusions, should have led to the crystallization of the high-temperature variety of serpentine, antigorite, at $T < 690$ °C, antigorite + brucite at $T < 350$ °C, and then lizardite + brucite at $T < 350$ °C. However, no

indications of high-temperature antigorite were identified in the inclusions, with only low-temperature varieties of serpentine being present, i.e., lizardite with a chrysotile admixture, with a stability range of 300–50 °C.

In total, from our point of view, data on water solubility in carbonatite melts [185] and temperature stability of serpentine polymorphs [173–175] indicate that only 0.5 wt% of magmatic water could have led to chrysotile crystallization in the CMIs at temperatures below 300 °C. As a result, we suppose that the remaining 2 wt% of water in the inclusions, which gave rise to the crystallization of brucite and lizardite could have come from an external source at a temperature below 300 °C.

Regardless of whether the water supply was predominantly external or deuteric, the serpentinization of individual inclusions should significantly modify both the mineral association of individual inclusions and the bulk composition of these inclusions. It is widely known that nyerereite, gregoryite, alkali sulfates and chlorides are highly soluble in water, and this process occurs very quickly even at surface conditions, requiring no high temperatures and pressures (e.g., [187,188]). A perfect example is the critical alteration of sodic–carbonatite rocks of the Oldoinyo Lengai volcano under the influence of atmospheric precipitation. After the crystallization of the sodic–carbonatite lavas of Oldoinyo Lengai (whose major minerals are nyerereite and gregoryite, and a minor mineral is sylvite), these rocks reacted with meteoric waters under normal temperature and pressure. The reactions resulted in the destruction of Na–Ca-bearing carbonates and chloride. The rates of these reactions are very high: gregoryite and sylvite are destroyed in a matter of a few days to a few weeks, and nyerereite in the course of a few months. As a result of this process, the bulk chemical composition of the originally natrocarbonatite rocks changes dramatically, and nyerereite–gregoryite carbonatites are completely transformed into calcite carbonatites over a period of one to a few years (e.g., [187,188]).

We assume that the post-magmatic serpentinization at $T \leq 300$ °C partly destroyed primary magmatic daughter minerals within the CMIs, such as nyerereite, gregoryite, alkali sulfates and chlorides. This conclusion is directly supported by the presence of Na–Ca carbonates (e.g., nyerereite, shortite), alkali sulfates, and chlorides among the groundmass minerals in the non-serpentinized kimberlites of the Udachnaya–East pipe [79,180–182], whereas the partially serpentinized (to varying degrees) kimberlites of the same body lack all these minerals. On the other hand, the stability of various alkaline carbonates (Table 2) in aqueous fluids is not the same. Shortite, for example, is stable in aqueous fluids up to 250 °C and 3.2 GPa [189], which means that if serpentinization occurred at temperatures below 250 °C, shortite may be associated with serpentine within an individual CMI.

Table 4 (column 1) indicates the minimum volume content of carbonates ($\geq 61.8\%$), sulfates ($\geq 7.7\%$) and chlorides ($\geq 5.3\%$) within the CMIs. In Table 4 (column 2–5), we present several boundary calculations of how many carbonates, sulfates and chlorides may have been present within the CMIs, depending on the water source (deuteric or external) and type of olivine serpentinized (daughter or host). According to our estimates, the actual content of carbonates, sulfates and chlorides inside the inclusions could reach 77 vol.%, 9.5 vol.% and 6.7 vol.%, respectively. As emphasized above, the serpentinization of the CMIs should also lead to the destruction of certain Na-rich carbonates, sulfates and chlorides, i.e., the content of Na in the parental melt was actually higher than in our presented estimates, and this melt could have had Na rather than Ca or K specifics.

7. Conclusions

This paper provides a detailed mineralogical description of secondary crystallized melt inclusions (CMIs) within healed cracks in olivine of a coarse peridotite xenolith derived from the relatively shallow (~100 km) lithospheric mantle beneath the Baltic supercraton. The CMIs contain carbonates, sulfates, chlorides, phosphates, oxides, silicates and sulfides. The content of carbonates in the inclusions exceeds 62 vol.%. Among 11 carbonate mineral species, alkali-rich varieties are predominant, with 5 of them being Na-

rich (shortite, eitelite, bradleyite, northupite and burkeite) and 2 being Na-K-rich (nyerereite and gregoryite/natrite).

The amount of silicates (serpentine + tetraferriphlogopite) within the CMIs reaches 19 vol.%, which corresponds to the SiO₂ levels ≤ 9.6 wt% in the parental melt. However, these estimates of SiO₂ abundance are probably significantly overestimated due to the fact that the parental melt could have reacted with the olivine matrix, (Mg,Fe)₂SiO₄. Another issue with these estimates is that no daughter olivine was found in the inclusions, and it is not known for sure whether serpentine developed at the expense of the daughter olivine or along the walls of the inclusions at the expense of the host olivine. Several approaches demonstrate that out of a total content of H₂O ≤ 2.6 wt%, estimated from water-bearing minerals (serpentine + brucite + tetraferriphlogopite), only ≤ 0.6 wt% H₂O can be attributed to deuteritic water, whereas the remaining ~2 wt% H₂O probably come from an external source, i.e., the melt parental to the inclusions was water-poor. In general, serpentinization of individual inclusions by external fluids leads to the destruction of various Na-K-Ca-carbonates, alkali sulfates and chlorides, and, accordingly, to an underestimation of alkali (especially sodium), chlorine and sulfur abundances in the bulk composition of inclusions.

In summary, this study provides direct evidence for the existence of Cl-S-P-rich alkaline-carbonate melt(s) in the shallow lithospheric mantle beneath the Baltic supercraton. The studied CMIs are suggested to have a genetic link with the magmatic event that finally formed the V. Grib kimberlite pipe. Exactly the same associations of daughter minerals were identified previously within secondary CMIs in olivine of sheared peridotite xenoliths from the Udachnaya-East and Komsomolskaya-Magnitnaya kimberlite pipes (Siberian craton), as well as from the Bultfontein kimberlite pipe in South Africa (Kapaavaal craton) [20,67–72]. In this type of mantle xenolith, the olivine-hosted CMIs are also dominated by carbonates, especially alkaline carbonate varieties. Therefore, melt inclusion studies of mantle xenoliths from kimberlites clearly demonstrate that carbonate-rich melts are far more widespread in the mantle than previously thought. It appears that Cl-S-P-rich alkaline-carbonate liquids played a crucial role at various stages of the kimberlite life cycle. Our results indicate that Cl-S-P-rich alkaline-carbonate melts can be effective metasomatic agents in the lithospheric mantle and participate in many processes of its evolution as well as in the Earth's carbon cycle, as demonstrated by many previous studies that dealt with the crystallization of lithospheric and sublithospheric diamonds.

Author Contributions: Project idea, A.V.G.; conceptualization, A.V.G., A.A.T. and E.V.A.; field work, E.V.A.; investigation and analytical work, A.A.T., E.V.A. and A.V.G.; interpretation of analytical data, A.A.T., A.V.G. and E.V.A.; data curation, A.V.G.; writing—original draft preparation, A.V.G., A.A.T. and E.V.A.; writing—review and editing, A.V.G., A.A.T. and E.V.A.; visualization, A.A.T.; supervision, A.V.G.; project administration, A.V.G.; funding acquisition, E.V.A. All authors have read and agreed to the published version of the manuscript.

Funding: All analytical works were supported by the Russian Science Foundation (grant No. 20-77-10018, <https://rscf.ru/project/20-77-10018/> accessed on 27 April 2023). The fieldwork and sampling were performed on state assignment of IGM SB RAS (No. 122041400157-9).

Data Availability Statement: The data are presented in this article.

Acknowledgments: We are grateful to two anonymous reviewers for their constructive and thoughtful comments; N.S. Karmanov, M.V. Khlestov A.V. Korsakov (IGM SB RAS) for assistance in the analytical works and Raman mapping.

Conflicts of Interest: The authors declare no conflict of interest.

References

1. Kelemen, P.B.; Hart, S.R.; Bernstein, S. Silica enrichment in the continental upper mantle via melt/rock reaction. *Earth Planet. Sci. Lett.* **1998**, *164*, 387–406. [[CrossRef](#)]
2. Grégoire, M.; Bell, D.R.; Le Roex, A.P. Garnet lherzolites from the Kaapvaal Craton (South Africa): Trace element evidence for a metasomatic history. *J. Petrol.* **2003**, *44*, 629–657. [[CrossRef](#)]

3. Burgess, S.R.; Harte, B.E.N. Tracing lithosphere evolution through the analysis of heterogeneous G9–G10 garnets in peridotite xenoliths, II: REE chemistry. *J. Petrol.* **2004**, *45*, 609–633. [[CrossRef](#)]
4. Simon, N.S.C.; Carlson, R.W.; Pearson, D.G.; Davies, G.R. The origin and evolution of the Kaapvaal cratonic lithospheric mantle. *J. Petrol.* **2007**, *48*, 589–625. [[CrossRef](#)]
5. Rehfeldt, T.; Foley, S.F.; Jacob, D.E.; Carlson, R.W.; Lowry, D. Contrasting types of metasomatism in dunite, wehrlite and websterite xenoliths from Kimberley, South Africa. *Geochim. Cosmochim. Acta* **2008**, *72*, 5722–5756. [[CrossRef](#)]
6. Gibson, S.A.; Malarkey, J.; Day, J.A. Melt depletion and enrichment beneath the western Kaapvaal Craton: Evidence from Finsch peridotite xenoliths. *J. Petrol.* **2008**, *49*, 1817–1852. [[CrossRef](#)]
7. Tang, Y.J.; Zhang, H.F.; Ying, J.F.; Su, B.X. Widespread refertilization of cratonic and circum-cratonic lithospheric mantle. *Earth Sci. Rev.* **2013**, *118*, 45–68. [[CrossRef](#)]
8. Agashev, A.M.; Ionov, D.A.; Pokhilenko, N.P.; Golovin, A.V.; Cherepanova, Y.; Sharygin, I.S. Metasomatism in lithospheric mantle roots: Constraints from whole-rock and mineral chemical composition of deformed peridotite xenoliths from kimberlite pipe Udachnaya. *Lithos* **2013**, *160*, 201–215. [[CrossRef](#)]
9. Doucet, L.S.; Ionov, D.A.; Golovin, A.V. The origin of coarse garnet peridotites in cratonic lithosphere: New data on xenoliths from the Udachnaya kimberlite, central Siberia. *Contrib. Mineral. Petrol.* **2013**, *165*, 1225–1242. [[CrossRef](#)]
10. Doucet, L.S.; Peslier, A.H.; Ionov, D.A.; Brandon, A.D.; Golovin, A.V.; Goncharov, A.G.; Ashchepkov, I.V. High water contents in the Siberian cratonic mantle linked to metasomatism: An FTIR study of Udachnaya peridotite xenoliths. *Geochim. Cosmochim. Acta* **2014**, *137*, 159–187. [[CrossRef](#)]
11. Howarth, G.H.; Barry, P.H.; Pernet-Fisher, J.F.; Baziotis, I.P.; Pokhilenko, N.P.; Pokhilenko, L.N.; Bodnar, R.J.; Taylor, L.A.; Agashev, A.M. Superplume metasomatism: Evidence from Siberian mantle xenoliths. *Lithos* **2014**, *184*, 209–224. [[CrossRef](#)]
12. Surgutanova, E.A.; Agashev, A.M.; Demonterova, E.I.; Golovin, A.V.; Pokhilenko, N.P. Sr and Nd isotope composition of deformed peridotite xenoliths from Udachnaya kimberlite pipe. *Dokl. Earth Sci.* **2016**, *471*, 1204–1207. [[CrossRef](#)]
13. Ionov, D.A.; Doucet, L.S.; Xu, Y.; Golovin, A.V.; Oleinikov, O.B. Reworking of Archean mantle in the NE Siberian craton by carbonatite and silicate melt metasomatism: Evidence from a carbonate-bearing, dunite-to-websterite xenolith suite from the Obnazhennaya kimberlite. *Geochim. Cosmochim. Acta* **2018**, *224*, 132–153. [[CrossRef](#)]
14. Ionov, D.A.; Qi, Y.H.; Kang, J.T.; Golovin, A.V.; Oleinikov, O.B.; Zheng, W.; Anbar, A.D.; Zhang, Z.F.; Huang, F. Calcium isotopic signatures of carbonatite and silicate metasomatism, melt percolation and crustal recycling in the lithospheric mantle. *Geochim. Cosmochim. Acta* **2019**, *248*, 1–13. [[CrossRef](#)]
15. Misra, K.C.; Anand, M.; Taylor, L.A.; Sobolev, N.V. Multi-stage metasomatism of diamondiferous eclogite xenoliths from the Udachnaya kimberlite pipe, Yakutia, Siberia. *Contrib. Mineral. Petrol.* **2004**, *146*, 696–714. [[CrossRef](#)]
16. Rezvukhin, D.I.; Alifirova, T.A.; Golovin, A.V.; Korsakov, A.V. A plethora of epigenetic minerals reveals a multistage metasomatic overprint of a mantle orthopyroxenite from the udachnaya kimberlite. *Minerals* **2020**, *10*, 264. [[CrossRef](#)]
17. Golovin, A.V.; Solovev, K.A.; Sharygin, I.S.; Letnikov, F.A. Aragonite in the Interstitial Space of a Mantle Xenolith from the Udachnaya Kimberlite Pipe (Siberian Craton): Direct Evidence for the Presence of Carbonatite Melts in the Deep Lithospheric Mantle. *Dokl. Earth Sci.* **2022**, *507*, 1044–1049. [[CrossRef](#)]
18. Bussweiler, Y. Polymineralic inclusions in megacrysts as proxies for kimberlite melt evolution—A review. *Minerals* **2019**, *9*, 530. [[CrossRef](#)]
19. Abersteiner, A.; Kamenetsky, V.S.; Goemann, K.; Golovin, A.V.; Sharygin, I.S.; Pearson, D.G.; Kamenetsky, M.; Gornova, M.A. Polymineralic inclusions in kimberlite-hosted megacrysts: Implications for kimberlite melt evolution. *Lithos* **2019**, *336*, 310–325. [[CrossRef](#)]
20. Golovin, A.V.; Kamenetsky, V.S. Compositions of kimberlite melts: A review of melt inclusions in kimberlite minerals. *Petrology* **2023**, *31*, 175–210. [[CrossRef](#)]
21. Rudnick, R.L.; McDonough, W.F.; Chappell, B.W. Carbonatite metasomatism in the northern Tanzanian mantle: Petrographic and geochemical characteristics. *Earth Planet. Sci. Lett.* **1993**, *114*, 463–475. [[CrossRef](#)]
22. Yaxley, G.M.; Green, D.H.; Kamenetsky, V. Carbonatite metasomatism in the southeastern Australian lithosphere. *J. Petrol.* **1998**, *39*, 1917–1930. [[CrossRef](#)]
23. Shu, Q.; Brey, G.P. Ancient mantle metasomatism recorded in subcalcic garnet xenocrysts: Temporal links between mantle metasomatism, diamond growth and crustal tectonomagmatism. *Earth Planet. Sci. Lett.* **2015**, *418*, 27–39. [[CrossRef](#)]
24. Pokhilenko, N.P.; Agashev, A.M.; Litasov, K.D.; Pokhilenko, L.N. Carbonatite metasomatism of peridotite lithospheric mantle: Implications for diamond formation and carbonatite-kimberlite magmatism. *Russ. Geol. Geophys.* **2015**, *56*, 280–295. [[CrossRef](#)]
25. Shchukina, E.V.; Agashev, A.M.; Pokhilenko, N.P. Metasomatic origin of garnet xenocrysts from the V. Grib kimberlite pipe, Arkhangelsk region, NW Russia. *Geosci. Front.* **2017**, *8*, 641–651. [[CrossRef](#)]
26. Liu, Z.; Ionov, D.A.; Nimis, P.; Xu, Y.; He, P.; Golovin, A.V. Thermal and compositional anomalies in a detailed xenolith-based lithospheric mantle profile of the Siberian craton and the origin of seismic midlithosphere discontinuities. *Geology* **2022**, *50*, 891–896. [[CrossRef](#)]
27. Klein-BenDavid, O.; Wirth, R.; Navon, O. TEM imaging and analysis of microinclusions in diamonds: A close look at diamond-growing fluids. *Am. Mineral.* **2006**, *91*, 353–365. [[CrossRef](#)]
28. Klein-BenDavid, O.; Izraeli, E.S.; Hauri, E.; Navon, O. Fluid inclusions in diamonds from the Diavik mine, Canada and the evolution of diamond-forming fluids. *Geochim. Cosmochim. Acta* **2007**, *71*, 723–744. [[CrossRef](#)]

29. Klein-BenDavid, O.; Logvinova, A.M.; Schrauder, M.; Spetius, Z.V.; Weiss, Y.; Hauri, E.H.; Kaminsky, F.V.; Sobolev, N.V.; Navon, O. High-Mg carbonatitic microinclusions in some Yakutian diamonds—A new type of diamond-forming fluid. *Lithos* **2009**, *112*, 648–659. [[CrossRef](#)]
30. Zedgenizov, D.A.; Ragozin, A.L.; Shatsky, V.S. Chloride-carbonate fluid in diamonds from the eclogite xenolith. *Dokl. Earth Sci.* **2007**, *415*, 961–964. [[CrossRef](#)]
31. Zedgenizov, D.A.; Rege, S.; Griffin, W.L.; Kagi, H.; Shatsky, V.S. Composition of trapped fluids in cuboid fibrous diamonds from the Udachnaya kimberlite: LAM-ICPMS analysis. *Chem. Geol.* **2007**, *240*, 151–162. [[CrossRef](#)]
32. Zedgenizov, D.A.; Ragozin, A.L.; Shatsky, V.S.; Araujo, D.; Griffin, W.L.; Kagi, H. Mg and Fe-rich carbonate–silicate high-density fluids in cuboid diamonds from the Internationalnaya kimberlite pipe (Yakutia). *Lithos* **2009**, *112*, 638–647. [[CrossRef](#)]
33. Zedgenizov, D.A.; Ragozin, A.L.; Shatsky, V.S.; Griffin, W.L. Diamond formation during metasomatism of mantle eclogite by chloride-carbonate melt. *Contrib. Mineral. Petrol.* **2018**, *173*, 84. [[CrossRef](#)]
34. Weiss, Y.; Kessel, R.; Griffin, W.L.; Kiflawi, I.; Klein-BenDavid, O.; Bell, D.R.; Harris, J.W.; Navon, O. A new model for the evolution of diamond-forming fluids: Evidence from microinclusion-bearing diamonds from Kankan, Guinea. *Lithos* **2009**, *112*, 660–674. [[CrossRef](#)]
35. Weiss, Y.; Czas, J.; Navon, O. Fluid inclusions in fibrous diamonds. *Rev. Mineral. Geochem.* **2022**, *88*, 475–532. [[CrossRef](#)]
36. Zedgenizov, D.A.; Malkovets, V.G.; Griffin, W.L. Composition of diamond-forming media in cuboid diamonds from the V. Grib kimberlite pipe (Arkhangelsk province, Russia). *Geochem. J.* **2017**, *51*, 205–213. [[CrossRef](#)]
37. Stachel, T.; Aulbach, S.; Harris, J.W. Mineral inclusions in lithospheric diamonds. *Rev. Mineral. Geochem.* **2022**, *88*, 307–391. [[CrossRef](#)]
38. Smith, E.M.; Krebs, M.Y.; Genzel, P.-T.; Brenker, F.E. Raman identification of inclusions in diamond. *Rev. Mineral. Geochem.* **2022**, *88*, 451–473. [[CrossRef](#)]
39. Logvinova, A.M.; Shatskiy, A.; Wirth, R.; Tomilenko, A.A.; Ugap'eva, S.S.; Sobolev, N.V. Carbonatite melt in type Ia gem diamond. *Lithos* **2019**, *342*, 463–467. [[CrossRef](#)]
40. Logvinova, A.M.; Wirth, R.; Zedgenizov, D.A.; Taylor, L.A. Carbonate–silicate–sulfide polyphase inclusion in diamond from the Komsomolskaya Kimberlite Pipe, Yakutia. *Geochem. Int.* **2018**, *56*, 283–291. [[CrossRef](#)]
41. Brenker, F.E.; Vollmer, C.; Vincze, L.; Vekemans, B.; Szymanski, A.; Janssens, K.; Szaloki, I.; Nasdala, L.; Joswig, W.; Kaminsky, F. Carbonates from the lower part of transition zone or even the lower mantle. *Earth Planet. Sci. Lett.* **2007**, *260*, 1–9. [[CrossRef](#)]
42. Kaminsky, F.; Wirth, R.; Matsyuk, S.; Schreiber, A.; Thomas, R. Nyerereite and nahcolite inclusions in diamond: Evidence for lower-mantle carbonatitic magmas. *Mineral. Mag.* **2009**, *73*, 797–816. [[CrossRef](#)]
43. Kaminsky, F. Mineralogy of the lower mantle: A review of 'super-deep' mineral inclusions in diamond. *Earth Sci. Rev.* **2012**, *110*, 127–147. [[CrossRef](#)]
44. Kaminsky, F.V.; Ryabchikov, I.D.; Wirth, R. A primary natrocarbonatitic association in the Deep Earth. *Mineral. Petrol.* **2016**, *110*, 387–398. [[CrossRef](#)]
45. Kaminsky, F.V.; Wirth, R.; Schreiber, A. Carbonatitic inclusions in deep mantle diamond from Juina, Brazil: New minerals in the carbonate-halide association. *Can. Mineral.* **2013**, *51*, 669–688. [[CrossRef](#)]
46. Wirth, R.; Kaminsky, F.; Matsyuk, S.; Schreiber, A. Unusual micro- and nano-inclusions in diamonds from the Juina Area, Brazil. *Earth Planet. Sci. Lett.* **2009**, *286*, 292–303. [[CrossRef](#)]
47. Sweeney, R.J. Carbonatite melt compositions in the Earth's mantle. *Earth Planet. Sci. Lett.* **1994**, *128*, 259–270. [[CrossRef](#)]
48. Sokol, A.G.; Kruk, A.N.; Chebotarev, D.A.; Palyanov, Y.N.; Sobolev, N.V. Conditions of carbonation and wehrlitization of lithospheric peridotite upon interaction with carbonatitic melts. *Dokl. Earth Sci.* **2015**, *465*, 1262–1267. [[CrossRef](#)]
49. Sokol, A.G.; Kruk, A.N.; Chebotarev, D.A.; Palyanov, Y.N. Carbonatite melt–peridotite interaction at 5.5–7.0 GPa: Implications for metasomatism in lithospheric mantle. *Lithos* **2016**, *248*, 66–79. [[CrossRef](#)]
50. Kruk, A.N.; Sokol, A.G.; Chebotarev, D.A.; Palyanov, Y.A.; Sobolev, N.V. Composition of a carbonatitic melt in equilibrium with lherzolite at 5.5–6.3 GPa and 1350 °C. *Dokl. Earth Sci.* **2016**, *467*, 303–307. [[CrossRef](#)]
51. Shatskiy, A.; Litasov, K.D.; Sharygin, I.S.; Ohtani, E. Composition of primary kimberlite melt in a garnet lherzolite mantle source: Constraints from melting phase relations in anhydrous Udachnaya-East kimberlite with variable CO₂ content at 6.5 GPa. *Gondwana Res.* **2017**, *45*, 208–227. [[CrossRef](#)]
52. Shatskiy, A.; Arefiev, A.V.; Podborodnikov, I.V.; Litasov, K.D. Origin of K-rich diamond-forming immiscible melts and CO₂ fluid via partial melting of carbonated pelites at a depth of 180–200 km. *Gondwana Res.* **2019**, *75*, 154–171. [[CrossRef](#)]
53. Shatskiy, A.; Bekhtenova, A.; Podborodnikov, I.V.; Arefiev, A.V.; Litasov, K.D. Metasomatic interaction of the eutectic Na- and K-bearing carbonate melts with natural garnet lherzolite at 6 GPa and 1100–1200 °C: Toward carbonatite melt composition in SCLM. *Lithos* **2020**, *374*, 105725. [[CrossRef](#)]
54. Shatskiy, A.; Bekhtenova, A.; Podborodnikov, I.V.; Arefiev, A.V.; Litasov, K.D. Carbonate melt interaction with natural eclogite at 6 GPa and 1100–1200 °C: Implications for metasomatic melt composition in subcontinental lithospheric mantle. *Chem. Geol.* **2020**, *558*, 119915. [[CrossRef](#)]
55. Shatskiy, A.; Bekhtenova, A.; Podborodnikov, I.V.; Arefiev, A.V.; Litasov, K.D. Towards composition of carbonatite melts in peridotitic mantle. *Earth Planet. Sci. Lett.* **2022**, *581*, 117395. [[CrossRef](#)]
56. Shatskiy, A.; Bekhtenova, A.; Arefiev, A.V.; Litasov, K.D. Melt Composition and Phase Equilibria in the Eclogite-Carbonate System at 6 GPa and 900–1500 °C. *Minerals* **2023**, *13*, 82. [[CrossRef](#)]

57. Dalton, J.A.; Presnall, D.C. The continuum of primary carbonatitic–kimberlitic melt compositions in equilibrium with lherzolite: Data from the system CaO–MgO–Al₂O₃–SiO₂–CO₂ at 6 GPa. *J. Petrol.* **1998**, *39*, 1953–1964. [[CrossRef](#)]
58. Safonov, O.G.; Kamenetsky, V.S.; Perchuk, L.L. Links between carbonatite and kimberlite melts in chloride–carbonate–silicate systems: Experiments and application to natural assemblages. *J. Petrol.* **2011**, *52*, 1307–1331. [[CrossRef](#)]
59. Kiseeva, E.S.; Yaxley, G.M.; Hermann, J.; Litasov, K.D.; Rosenthal, A.; Kamenetsky, V.S. An experimental study of carbonated eclogite at 3–5–5 GPa—Implications for silicate and carbonate metasomatism in the cratonic mantle. *J. Petrol.* **2012**, *53*, 727–759. [[CrossRef](#)]
60. Kiseeva, E.S.; Litasov, K.D.; Yaxley, G.M.; Ohtani, E.; Kamenetsky, V.S. Melting and phase relations of carbonated eclogite at 9–21 GPa and the petrogenesis of alkali-rich melts in the deep mantle. *J. Petrol.* **2013**, *54*, 1555–1583. [[CrossRef](#)]
61. Litasov, K.D.; Shatskiy, A.; Ohtani, E.; Yaxley, G.M. Solidus of alkaline carbonatite in the deep mantle. *Geology* **2013**, *41*, 79–82. [[CrossRef](#)]
62. Shatskiy, A.; Podborodnikov, I.V.; Arefiev, A.V.; Bekhtenova, A.; Vinogradova, Y.G.; Stepanov, K.M.; Litasov, K.D. Pyroxene-carbonate reactions in the CaMgSi₂O₆±NaAlSi₂O₆+ MgCO₃±Na₂CO₃±K₂CO₃ system at 3–6 GPa: Implications for partial melting of carbonated peridotite. *Contrib. Mineral. Petrol.* **2021**, *176*, 34. [[CrossRef](#)]
63. Timmerman, S.; Spivak, A.V.; Jones, A.P. Carbonatitic melts and their role in diamond formation in the deep Earth. *Elements* **2021**, *17*, 321–326. [[CrossRef](#)]
64. Green, D.H.; Wallace, M.E. Mantle metasomatism by ephemeral carbonatite melts. *Nature* **1988**, *336*, 459–462. [[CrossRef](#)]
65. Giuliani, A.; Kamenetsky, V.S.; Phillips, D.; Kendrick, M.A.; Wyatt, B.A.; Goemann, K. Nature of alkali-carbonate fluids in the sub-continental lithospheric mantle. *Geology* **2012**, *40*, 967–970. [[CrossRef](#)]
66. Sparks, R.S.J.; Brooker, R.A.; Field, M.; Kavanagh, J.; Schumacher, J.C.; Walter, M.J.; White, J. The nature of erupting kimberlite melts. *Lithos* **2009**, *112*, 429–438. [[CrossRef](#)]
67. Golovin, A.V.; Sharygin, I.S.; Korsakov, A.V. Origin of alkaline carbonates in kimberlites of the Siberian craton: Evidence from melt inclusions in mantle olivine of the Udachnaya-East pipe. *Chem. Geol.* **2017**, *455*, 357–375. [[CrossRef](#)]
68. Golovin, A.V.; Sharygin, I.S.; Kamenetsky, V.S.; Korsakov, A.V.; Yaxley, G.M. Alkali-carbonate melts from the base of cratonic lithospheric mantle: Links to kimberlites. *Chem. Geol.* **2018**, *483*, 261–274. [[CrossRef](#)]
69. Golovin, A.V.; Sharygin, I.S.; Korsakov, A.V.; Kamenetsky, V.S.; Abersteiner, A. Can primitive kimberlite melts be alkali-carbonate liquids: Composition of the melt snapshots preserved in deepest mantle xenoliths. *J. Raman Spectrosc.* **2020**, *51*, 1849–1867. [[CrossRef](#)]
70. Sharygin, I.S.; Golovin, A.V.; Dymshits, A.M.; Kalugina, A.D.; Solovev, K.A.; Malkovets, V.G.; Pokhilenko, N.P. Relics of Deep Alkali–Carbonate Melt in the Mantle Xenolith from the Komsomolskaya–Magnitnaya Kimberlite Pipe (Upper Muna Field, Yakutia). *Dokl. Earth Sci.* **2021**, *500*, 842–847. [[CrossRef](#)]
71. Sharygin, I.S.; Golovin, A.V.; Tarasov, A.A.; Dymshits, A.M.; Kovaleva, E. Confocal Raman spectroscopic study of melt inclusions in olivine of mantle xenoliths from the Bultfontein kimberlite pipe (Kimberley cluster, South Africa): Evidence for alkali-rich carbonate melt in the mantle beneath Kaapvaal Craton. *J. Raman Spectrosc.* **2022**, *53*, 508–524. [[CrossRef](#)]
72. Tarasov, A.A.; Golovin, A.V.; Sharygin, I.S. Alkali-containing minerals within melt inclusions in olivine of mantle xenoliths from Bulfontein kimberlite pipe) Kaapvaal Craton): Evidence on high concentrations of alkalis in kimberlite melts. *Geodyn. Tectonophys.* **2022**, *13*, 0662. [[CrossRef](#)]
73. Golovin, A.V.; Sharygin, V.V.; Pokhilenko, N.P.; Mal'kovets, V.G.; Sobolev, N.V.; Kolesov, B.A. Secondary melt inclusions in olivine from unaltered kimberlites of the Udachnaya-East pipe, Yakutia. *Dokl. Earth Sci.* **2003**, *388*, 93–96.
74. Golovin, A.V.; Sharygin, V.V.; Pokhilenko, N.P. Melt inclusions in olivine phenocrysts in unaltered kimberlites from the Udachnaya-East pipe, Yakutia: Some aspects of kimberlite magma evolution during late crystallization stages. *Petrology* **2007**, *15*, 168–183. [[CrossRef](#)]
75. Kamenetsky, M.B.; Sobolev, A.V.; Kamenetsky, V.S.; Maas, R.; Danyushevsky, L.V.; Thomas, R.; Pokhilenko, N.P.; Sobolev, N.V. Kimberlite melts rich in alkali chlorides and carbonates: A potent metasomatic agent in the mantle. *Geology* **2004**, *32*, 845–848. [[CrossRef](#)]
76. Kamenetsky, V.S.; Kamenetsky, M.B.; Weiss, Y.; Navon, O.; Nielsen, T.F.D. How unique is the Udachnaya-East kimberlite? Comparison with kimberlites from the Slave Craton (Canada) and SW Greenland. *Lithos* **2009**, *112*, 334–346. [[CrossRef](#)]
77. Kamenetsky, V.S.; Grütter, H.; Kamenetsky, M.B.; Gömann, K. Parental carbonatitic melt of the Koala kimberlite (Canada): Constraints from melt inclusions in olivine and Cr-spinel, and groundmass carbonate. *Chem. Geol.* **2013**, *353*, 96–111. [[CrossRef](#)]
78. Abersteiner, A.; Giuliani, A.; Kamenetsky, V.S.; Phillips, D. Petrographic and melt-inclusion constraints on the petrogenesis of a magmaclast from the Venetia kimberlite cluster, South Africa. *Chem. Geol.* **2017**, *455*, 331–341. [[CrossRef](#)]
79. Abersteiner, A.; Kamenetsky, V.S.; Golovin, A.V.; Kamenetsky, M.; Goemann, K. Was Crustal Contamination Involved in the Formation of the Serpentine-Free Udachnaya-East Kimberlite? New Insights into Parental Melts, Liquidus Assemblage and Effects of Alteration. *J. Petrol.* **2018**, *59*, 1467–1492. [[CrossRef](#)]
80. Abersteiner, A.; Kamenetsky, V.S.; Kamenetsky, M.; Goemann, K.; Ehrig, K.; Rodemann, T. Significance of halogens (F, Cl) in kimberlite melts: Insights from mineralogy and melt inclusions in the Roger pipe (Ekati, Canada). *Chem. Geol.* **2018**, *478*, 148–163. [[CrossRef](#)]

81. Abersteiner, A.; Kamenetsky, V.S.; Goemann, K.; Giuliani, A.; Howarth, G.H.; Castillo-Oliver, M.; Thompson, J.; Kamenetsky, M.; Cherry, A. Composition and emplacement of the Benfontein kimberlite sill complex (Kimberley, South Africa): Textural, petrographic and melt inclusion constraints. *Lithos* **2019**, *324–325*, 297–314. [[CrossRef](#)]
82. Abersteiner, A.; Kamenetsky, V.S.; Goemann, K.; Golovin, A.V.; Sharygin, I.S.; Giuliani, A.; Rodemann, T.; Spetsius, Z.V.; Kamenetsky, M. Djerfisherite in kimberlites and their xenoliths: Implications for kimberlite melt evolution. *Contrib. Mineral. Petrol.* **2019**, *174*, 8. [[CrossRef](#)]
83. Abersteiner, A.; Kamenetsky, V.S.; Goemann, K.; Kjarsgaard, B.A.; Fedortchouk, Y.; Ehrig, K.; Kamenetsky, M. Evolution of kimberlite magmas in the crust: A case study of groundmass and mineral-hosted inclusions in the Mark kimberlite (Lac de Gras, Canada). *Lithos* **2020**, *372–373*, 105690. [[CrossRef](#)]
84. Abersteiner, A.; Kamenetsky, V.S.; Goemann, K.; Golovin, A.; Kamenetsky, M. Olivine in Kimberlites: Magma Evolution from Deep Mantle to Eruption. *J. Petrol.* **2022**, *63*, egac055. [[CrossRef](#)]
85. Schiano, P.; Clocchiatti, R. Worldwide occurrence of silica-rich melts in sub-continental and sub-oceanic mantle minerals. *Nature* **1994**, *368*, 621–624. [[CrossRef](#)]
86. Andersen, T.; Neumann, E.-R. Fluid inclusions in mantle xenoliths. *Lithos* **2001**, *55*, 301–320. [[CrossRef](#)]
87. Frezzotti, M.-L. Silicate-melt inclusions in magmatic rocks: Applications to petrology. *Lithos* **2001**, *55*, 273–299. [[CrossRef](#)]
88. Golovin, A.V.; Sharygin, V.V. Petrogenetic analysis of fluid and melt inclusions in minerals from mantle xenoliths from the Bele pipe basanites (North Minusa depression). *Russ. Geol. Geophys.* **2007**, *48*, 811–824. [[CrossRef](#)]
89. Maitre, R.W.L.; Streckeisen, A.; Zanettin, B.; Le Bas, M.J.; Bonin, B.; Bateman, P.; Bellieni, G.; Dudek, A.; Efremova, S.; Keller, J.; et al. *Igneous Rocks. A Classification and Glossary of Terms: Recommendations of the International Union of Geological Sciences Subcommission on the Systematics of Igneous Rocks*; Cambridge University Press: Cambridge, UK, 2002; Volume 2.
90. Mitchell, R.H. Carbonatites and carbonatites and carbonatites. *Can. Mineral.* **2005**, *43*, 2049–2068. [[CrossRef](#)]
91. Shevchenko, S.S.; Lokhov, K.I.; Sergeev, S.A. Isotope studies in VSEGEI. Prospects of application of results for predicting and search of diamond deposits. In Proceedings of the Scientific Practical Conference on Efficiency of Prediction and Search for Diamond Deposits: Past, Present, and Future, Saint-Petersburg, Russia, 25–27 May 2004; pp. 383–387.
92. Larionova, Y.O.; Sazonova, L.V.; Lebedeva, N.M.; Nosova, A.A.; Tretyachenko, V.V.; Travin, A.V.; Kargin, A.V.; Yudin, D.S. Kimberlite age in the Arkhangelsk Province, Russia: Isotopic geochronologic Rb–Sr and $^{40}\text{Ar}/^{39}\text{Ar}$ and mineralogical data on phlogopite. *Petrology* **2016**, *24*, 562–593. [[CrossRef](#)]
93. Shchukina, E.V.; Agashev, A.M.; Kostrovitsky, S.I.; Pokhilenko, N.P. Metasomatic processes in the lithospheric mantle beneath the V. Grib kimberlite pipe (Arkhangelsk diamondiferous province, Russia). *Russ. Geol. Geophys.* **2015**, *56*, 1701–1716. [[CrossRef](#)]
94. Gudimova, A.I.; Agasheva, E.V.; Agashev, A.M.; Pokhilenko, N.V. Composition, Structure, and Thermal Regime of the Lithospheric Mantle in the Area of the Highly Diamondiferous V. Grib Kimberlite Pipe, Arkhangelsk Diamondiferous Province: Data on the Chemical Composition of Garnet and Chrome-Diopside Xenocrysts. *Dokl. Earth Sci.* **2022**, *505*, 439–445. [[CrossRef](#)]
95. Bogatkov, O.A.; Kononova, V.A.; Nosova, A.A.; Kondrashov, I.A. Kimberlites and lamproites of the East European Platform: Petrology and geochemistry. *Petrology* **2007**, *15*, 315–334. [[CrossRef](#)]
96. Kononova, V.A.; Golubeva, Y.Y.; Bogatkov, O.A.; Kargin, A.V. Diamond resource potential of kimberlites from the Zimny Bereg field, Arkhangel'sk oblast. *Geol. Ore Depos.* **2007**, *49*, 421–441. [[CrossRef](#)]
97. Mahotkin, I.L.; Gibson, S.A.; Thompson, R.N.; Zhuravlev, D.Z.; Zherdev, P.U. Late Devonian Diamondiferous Kimberlite and Alkaline Picrite (Proto-kimberlite?) Magmatism in the Arkhangelsk Region, NW Russia. *J. Petrol.* **2000**, *41*, 201–227. [[CrossRef](#)]
98. Agasheva, E.V. Magmatic Material in Sandstone Shows Potential for New Diamond Deposits within the Northern East European Platform. *Minerals* **2021**, *11*, 339. [[CrossRef](#)]
99. Golubeva, Y.Y.; Pervov, V.A.; Kononova, V.A. Petrogenesis of autoliths from kimberlitic breccias in the V. Grib Pipe (Arkhangelsk district). *Dokl. Earth Sci.* **2006**, *411*, 1257–1262. [[CrossRef](#)]
100. Shchukina, E.V.; Shchukin, V.S. Diamond Exploration Potential of the Northern East European Platform. *Minerals* **2018**, *8*, 189. [[CrossRef](#)]
101. Shchukina, E.V.; Agashev, A.M.; Shchukin, V. Diamond-Bearing Root Beneath the Northern East European Platform (Arkhangelsk Region, Russia): Evidence from Cr-Pyrope Trace-Element Geochemistry. *Minerals* **2019**, *9*, 261. [[CrossRef](#)]
102. Taylor, W.R. An experimental test of some geothermometer and geobarometer formulations for upper mantle peridotites with application to the thermobarometry of fertile lherzolite and garnet websterite. *Neues Jahrb. Mineral.-Abh.* **1998**, *172*, 381–408.
103. Nickel, K.G.; Green, D.H. Empirical geothermobarometry for garnet peridotites and implications for the nature of the lithosphere, kimberlites and diamonds. *Earth Planet. Sci. Lett.* **1985**, *73*, 158–170. [[CrossRef](#)]
104. Dziewonski, A.M.; Anderson, D.L. Preliminary reference Earth model. *Phys. Earth Planet. Inter.* **1981**, *25*, 297–356. [[CrossRef](#)]
105. Shchukina, E.V.; Golovin, N.N.; Mal'kovets, V.G.; Pokhilenko, N.P. Mineralogy and equilibrium P-T estimates for peridotite assemblages from the V. Grib kimberlite pipe (Arkhangelsk Kimberlite Province). *Dokl. Earth Sci.* **2012**, *444*, 776–781. [[CrossRef](#)]
106. Sobolev, N.V.; Lavrent'ev, Y.G.; Pokhilenko, N.P.; Usova, L.V. Chrome-rich garnets from the kimberlites of Yakutia and their parageneses. *Contrib. Mineral. Petrol.* **1973**, *40*, 39–52. [[CrossRef](#)]
107. Grütter, H.S.; Gurney, J.J.; Menzies, A.H.; Winter, F. An updated classification scheme for mantle-derived garnet, for use by diamond explorers. *Lithos* **2004**, *77*, 841–857. [[CrossRef](#)]
108. Streckeisen, A.L. Plutonic rocks: Classification and nomenclature recommended by the I.U.G.S. Sub commission on the systematic of Igneous Rocks. *Geotimes* **1973**, *18*, 26–30.

109. Walter, M.J. Melting of Garnet Peridotite and the Origin of Komatiite and Depleted Lithosphere. *J. Petrol.* **1998**, *39*, 29–60. [[CrossRef](#)]
110. O'Neill, H.S.C.; Wood, B.J. An experimental study of Fe-Mg partitioning between garnet and olivine and its calibration as a geothermometer. *Contrib. Mineral. Petrol.* **1979**, *70*, 59–70. [[CrossRef](#)]
111. Hasterok, D.; Chapman, D.S. Heat production and geotherms for the continental lithosphere. *Earth Planet. Sci. Lett.* **2011**, *307*, 59–70. [[CrossRef](#)]
112. Korolyuk, V.N.; Lavrent'ev, Y.G.; Usova, L.V.; Nigmatulina, E.N. JXA-8100 microanalyzer: Accuracy of analysis of rock-forming minerals. *Russ. Geol. Geophys.* **2008**, *49*, 165–168. [[CrossRef](#)]
113. Lavrent'ev, Y.G.; Korolyuk, V.N.; Usova, L.V.; Nigmatulina, E.N. Electron probe microanalysis of rock-forming minerals with a JXA-8100 electron probe microanalyzer. *Russ. Geol. Geophys.* **2015**, *56*, 1428–1436. [[CrossRef](#)]
114. Lafuente, B.; Downs, R.T.; Yang, H.; Stone, N. The power of databases: The RRUFF project. In *Highlights in Mineralogical Crystallography*; Thomas, A., Rosa Micaela, D., Eds.; De Gruyter (O): Berlin, Germany; München, Germany; Boston, MA, USA, 2016; pp. 1–30.
115. Bolotina, N.B.; Gavryushkin, P.N.; Korsakov, A.V.; Rashchenko, S.V.; Seryotkin, Y.V.; Golovin, A.V.; Moine, B.N.; Zaitsev, A.N.; Litasov, K.D. Incommensurately modulated twin structure of nyerereite $\text{Na}_{1.64}\text{K}_{0.36}\text{Ca}(\text{CO}_3)_2$. *Acta Crystallogr. B Struct. Sci. Cryst. Eng. Mater.* **2017**, *73*, 276–284. [[CrossRef](#)] [[PubMed](#)]
116. Golovin, A.V.; Korsakov, A.V.; Gavryushkin, P.N.; Zaitsev, A.N.; Thomas, V.G.; Moine, B.N. Raman spectra of nyerereite, gregoryite, and synthetic pure $\text{Na}_2\text{Ca}(\text{CO}_3)_2$: Diversity and application for the study micro inclusions. *J. Raman Spectrosc.* **2017**, *48*, 1559–1565. [[CrossRef](#)]
117. Warr, L.N. IMA–CNMNC approved mineral symbols. *Mineral. Mag.* **2021**, *85*, 291–320. [[CrossRef](#)]
118. Zaitsev, A.N.; Keller, J.; Spratt, J.; Jeffries, T.E.; Sharygin, V.V. Chemical composition of nyerereite and gregoryite from natrocarbonatites of Oldoinyo Lengai volcano, Tanzania. *Geol. Ore Depos.* **2009**, *51*, 608–616. [[CrossRef](#)]
119. Zucchini, A.; Gavryushkin, P.N.; Golovin, A.V.; Bolotina, N.B.; Stabile, P.; Carroll, M.R.; Comodi, P.; Frondini, F.; Morgavi, D.; Perugini, D.; et al. Crystal structure of nyerereite: A possible messenger from the deep Earth. *Am. Mineral.* **2022**, *107*, 2054–2064. [[CrossRef](#)]
120. Frost, R.L.; Dickfos, M.J. Raman and infrared spectroscopic study of the anhydrous carbonate minerals shortite and barytocalcite. *Spectrochim. Acta Part A* **2008**, *71*, 143–146. [[CrossRef](#)]
121. Buzgar, N.; Apopei, A.I. The Raman study of certain carbonates. *Geol. Tomul L* **2009**, *2*, 97–112.
122. Shatskiy, A.; Gavryushkin, P.N.; Sharygin, I.S.; Litasov, K.D.; Kupriyanov, I.N.; Higo, Y.; Borzdov, Y.M.; Funakoshi, K.; Palyanov, Y.N.; Ohtani, E. Melting and subsolidus phase relations in the system $\text{Na}_2\text{CO}_3\text{-MgCO}_3\pm\text{H}_2\text{O}$ at 6 GPa and the stability of $\text{Na}_2\text{Mg}(\text{CO}_3)_2$ in the upper mantle. *Am. Mineral.* **2013**, *98*, 2172–2182. [[CrossRef](#)]
123. Sharygin, I.S.; Golovin, A.V.; Korsakov, A.V.; Pokhilenko, N.P. Eitelite in sheared peridotite xenoliths from Udachnaya-East kimberlite pipe (Russia)—A new locality and host rock type. *Eur. J. Mineral.* **2013**, *25*, 825–834. [[CrossRef](#)]
124. Edwards, H.G.M.; Villar, S.E.J.; Jehlicka, J.; Munshi, T. FT-Raman spectroscopic study of calcium-rich and magnesium-rich carbonate minerals. *Spectrochim. Acta Part A* **2005**, *61*, 2273–2280. [[CrossRef](#)] [[PubMed](#)]
125. Perrin, J.; Vielzeuf, D.; Laporte, D.; Ricolleau, A.; Rossman, G.R.; Floquet, N. Raman characterization of synthetic magnesian calcites. *Am. Mineral.* **2016**, *101*, 2525–2538. [[CrossRef](#)]
126. Gao, J.; Huang, W.; Wu, X.; Fan, D.; Wu, Z.; Xia, D.; Qin, S. Compressibility of carbonophosphate bradleyite $\text{Na}_3\text{Mg}(\text{CO}_3)(\text{PO}_4)$ by X-ray diffraction and Raman spectroscopy. *Phys. Chem. Miner.* **2015**, *42*, 191–201. [[CrossRef](#)]
127. Kozlov, E.N.; Fomina, E.N.; Bocharov, V.N.; Sidorov, M.Y.; Vlasenko, N.S.; Shilovskikh, V.V. A Raman spectroscopic study of the natural carbonophosphates $\text{Na}_3\text{MCO}_3\text{PO}_4$ (M is Mn, Fe, and Mg). *Eur. J. Mineral.* **2021**, *33*, 283–297. [[CrossRef](#)]
128. Frost, R.L.; Dickfos, M.J. Raman spectroscopy of halogen-containing carbonates. *J. Raman Spectrosc.* **2007**, *38*, 1516–1522. [[CrossRef](#)]
129. Korsakov, A.V.; Golovin, A.V.; De Gussem, K.; Sharygin, I.S.; Vandenabeele, P. First finding of burkeite in melt inclusions in olivine from sheared lherzolite xenoliths. *Spectrochim. Acta Part A* **2009**, *73*, 424–427. [[CrossRef](#)]
130. Jentzsch, P.; Kampe, B.; Ciobotă, V.; Rösch, P.; Popp, J. Inorganic salts in atmospheric particulate matter: Raman spectroscopy as an analytical tool. *Spectrochim. Acta Part A* **2013**, *115*, 697–708. [[CrossRef](#)]
131. Buzgar, N.; Buzatu, A.; Sanislav, I.V. The Raman study on certain sulfates. *An. Stiint. U. Al. I-Ma* **2009**, *55*, 5–23.
132. Antonakos, A.; Liarokapis, E.; Leventouri, T. Micro-Raman and FTIR studies of synthetic and natural apatites. *Biomaterials* **2007**, *28*, 3043–3054. [[CrossRef](#)]
133. Shebanova, O.N.; Lazor, P. Raman spectroscopic study of magnetite (FeFe_2O_4): A new assignment for the vibrational spectrum. *J. Solid State Chem.* **2003**, *174*, 424–430. [[CrossRef](#)]
134. Korsakov, A.V.; Golovin, A.V.; Sharygin, I.S. Raman Spectroscopic Study of Micas from Ultra-Fresh Udachnaya-East Kimberlites. In Proceedings of the 11th International GeoRaman Conference, St Louis, MO, USA, 15–19 June 2014; p. 141.
135. Petriglieri, J.R.; Salvioli-Mariani, E.; Mantovani, L.; Tribaudino, M.; Lottici, P.P.; Laporte-Magoni, C.; Bersani, D. Micro-Raman mapping of the polymorphs of serpentine. *J. Raman Spectrosc.* **2015**, *46*, 953–958. [[CrossRef](#)]
136. Dawson, P.; Hadfield, C.D.; Wilkinson, G.R. The polarized infra-red and Raman spectra of $\text{Mg}(\text{OH})_2$ and $\text{Ca}(\text{OH})_2$. *J. Phys. Chem. Solids* **1973**, *34*, 1217–1225. [[CrossRef](#)]
137. Mercier, J.-C.C. Peridotite Xenoliths and the Dynamics of Kimberlite Intrusion. In *The Mantle Sample: Inclusion in Kimberlites and Other Volcanics*; American Geophysical Union: Washington, DC, USA, 1979; pp. 197–212.

138. Drury, M.R.; Roermund, H.L.M.V. Fluid Assisted Recrystallization in Upper Mantle Peridotite Xenoliths from Kimberlites. *J. Petrol.* **1989**, *30*, 133–152. [[CrossRef](#)]
139. O'Reilly, S.Y.; Griffin, W.L. The continental lithosphere–asthenosphere boundary: Can we sample it? *Lithos* **2010**, *120*, 1–13. [[CrossRef](#)]
140. Ionov, D.A.; Doucet, L.S.; Pogge von Strandmann, P.A.E.; Golovin, A.V.; Korsakov, A.V. Links between deformation, chemical enrichments and Li-isotope compositions in the lithospheric mantle of the central Siberian craton. *Chem. Geol.* **2017**, *475*, 105–121. [[CrossRef](#)]
141. Brett, R.C.; Russell, J.K.; Andrews, G.D.M.; Jones, T.J. The ascent of kimberlite: Insights from olivine. *Earth Planet. Sci. Lett.* **2015**, *424*, 119–131. [[CrossRef](#)]
142. Roedder, E. Fluid inclusions. *Rev. Mineral.* **1984**, *12*, 59–66.
143. Gualda, G.A.R.; Pamukcu, A.S.; Giorso, M.S.; Anderson, A.T., Jr.; Sutton, S.R.; Rivers, M.L. Timescales of Quartz Crystallization and the Longevity of the Bishop Giant Magma Body. *PLoS ONE* **2012**, *7*, e37492. [[CrossRef](#)]
144. Anderson, A.T.; Davis, A.M.; Lu, F. Evolution of Bishop Tuff Rhyolitic Magma Based on Melt and Magnetite Inclusions and Zoned Phenocrysts. *J. Petrol.* **2000**, *41*, 449–473. [[CrossRef](#)]
145. Jaoul, O.; Bertran-Alvarez, Y.; Liebermann, R.C.; Price, G.D. Fe-Mg interdiffusion in olivine up to 9 GPa at T = 600–900 °C; experimental data and comparison with defect calculations. *Phys. Earth Planet. Inter.* **1995**, *89*, 199–218. [[CrossRef](#)]
146. Kjarsgaard, B.A.; Pearson, D.G.; Tappe, S.; Nowell, G.M.; Dowall, D.P. Geochemistry of hypabyssal kimberlites from Lac de Gras, Canada: Comparisons to a global database and applications to the parent magma problem. *Lithos* **2009**, *112*, 236–248. [[CrossRef](#)]
147. Kamenetsky, V.S.; Kamenetsky, M.B.; Sobolev, A.V.; Golovin, A.V.; Demouchy, S.; Faure, K.; Sharygin, V.V.; Kuzmin, D.V. Olivine in the Udachnaya-East Kimberlite (Yakutia, Russia): Types, Compositions and Origins. *J. Petrol.* **2008**, *49*, 823–839. [[CrossRef](#)]
148. Kamenetsky, V.S.; Golovin, A.V.; Maas, R.; Giuliani, A.; Kamenetsky, M.B.; Weiss, Y. Towards a new model for kimberlite petrogenesis: Evidence from unaltered kimberlites and mantle minerals. *Earth Sci. Rev.* **2014**, *139*, 145–167. [[CrossRef](#)]
149. Nielsen, T.F.D.; Sand, K.K. The Majuagaa kimberlite dike, Maniitsoq region, west Greenland: Constraints on an mg-rich silicocarbonatitic melt composition from groundmass mineralogy and bulk compositions. *Can. Mineral.* **2008**, *46*, 1043–1061. [[CrossRef](#)]
150. Brett, R.C.; Russell, J.K.; Moss, S. Origin of olivine in kimberlite: Phenocryst or impostor? *Lithos* **2009**, *112*, 201–212. [[CrossRef](#)]
151. Arndt, N.T.; Guitreau, M.; Boullier, A.-M.; Le Roex, A.; Tommasi, A.; Cordier, P.; Sobolev, A. Olivine, and the Origin of Kimberlite. *J. Petrol.* **2010**, *51*, 573–602. [[CrossRef](#)]
152. Soltys, A.; Giuliani, A.; Phillips, D. A new approach to reconstructing the composition and evolution of kimberlite melts: A case study of the archetypal Bultfontein kimberlite (Kimberley, South Africa). *Lithos* **2018**, *304–307*, 1–15. [[CrossRef](#)]
153. Giuliani, A.; Pearson, D.G.; Soltys, A.; Dalton, H.; Phillips, D.; Foley, S.F.; Lim, E.; Goemann, K.; Griffin, W.L.; Mitchell, R.H. Kimberlite genesis from a common carbonate-rich primary melt modified by lithospheric mantle assimilation. *Sci. Adv.* **2020**, *6*, eaaz0424. [[CrossRef](#)]
154. Russell, J.K.; Porritt, L.A.; Lavallée, Y.; Dingwell, D.B. Kimberlite ascent by assimilation-fuelled buoyancy. *Nature* **2012**, *481*, 352–356. [[CrossRef](#)]
155. Chepurov, A.I.; Zhimulev, E.I.; Agafonov, L.V.; Sonin, V.M.; Chepurov, A.A.; Tomilenko, A.A. The stability of ortho- and clinopyroxenes, olivine, and garnet in kimberlitic magma. *Russ. Geol. Geophys.* **2013**, *54*, 406–415. [[CrossRef](#)]
156. Kamenetsky, V.S.; Yaxley, G.M. Carbonate–silicate liquid immiscibility in the mantle propels kimberlite magma ascent. *Geochim. Cosmochim. Acta* **2015**, *158*, 48–56. [[CrossRef](#)]
157. Stone, R.S.; Luth, R.W. Orthopyroxene survival in deep carbonatite melts: Implications for kimberlites. *Contrib. Mineral. Petrol.* **2016**, *171*, 63. [[CrossRef](#)]
158. Sharygin, I.S.; Litasov, K.D.; Shatskiy, A.; Safonov, O.G.; Golovin, A.V.; Ohtani, E.; Pokhilenko, N.P. Experimental constraints on orthopyroxene dissolution in alkali-carbonate melts in the lithospheric mantle: Implications for kimberlite melt composition and magma ascent. *Chem. Geol.* **2017**, *455*, 44–56. [[CrossRef](#)]
159. Kamenetsky, V.S.; Kamenetsky, M.B.; Sobolev, A.V.; Golovin, A.V.; Sharygin, V.V.; Pokhilenko, N.P.; Sobolev, N.V. Can pyroxenes be liquidus minerals in the kimberlite magma? *Lithos* **2009**, *112*, 213–222. [[CrossRef](#)]
160. Abersteiner, A.; Kamenetsky, V.S.; Golovin, A.; Goemann, K.; Ehrig, K. Dissolution of mantle orthopyroxene in kimberlitic melts: Petrographic, geochemical and melt inclusion constraints from an orthopyroxenite xenolith from the Udachnaya-East kimberlite (Siberian Craton, Russia). *Lithos* **2021**, *398–399*, 106331. [[CrossRef](#)]
161. Kinny, P.D.; Griffin, B.; Heaman, L.M.; Brakhfogel, F.F.; Spetsius, Z.V. SHRIMP U-Pb ages of perovskite from Yakutian kimberlites. *Russ. Geol. Geophys.* **1997**, *38*, 91–99.
162. Sarsadskih, N.N.; Blagulkina, V.A.; Silin, Y.I. On the absolute age of the Yakutian kimberlites. *Dokl. Akad. Nauk SSSR* **1966**, *168*, 420–423. (In Russian)
163. Zaitsev, A.; Smelov, A. *Isotope Geochronology of Rocks of the Yakutian Kimberlite Province*; DPMGI SB RAS: Yakutsk, Russia, 2010. (In Russian)
164. Kostrovitsky, S.I.; Solov'eva, L.V.; Yakovlev, D.A.; Suvorova, L.F.; Sandimirova, G.P.; Travin, A.V.; Yudin, D.S. Kimberlites and megacrystic suite: Isotope-geochemical studies. *Petrology* **2013**, *21*, 127–144. [[CrossRef](#)]
165. Davis, G.L. The ages and uranium contents of zircons from kimberlites and associated rocks. *Int. Kimberl. Conf.* **1977**, *2*, 67–69.

166. Kramers, J.D.; Roddick, J.C.M.; Dawson, J.B. Trace element and isotope studies on veined, metasomatic and “MARID” xenoliths from Bultfontein, South Africa. *Earth Planet. Sci. Lett.* **1983**, *65*, 90–106. [[CrossRef](#)]
167. Kalugina, A.; Sharygin, I.; Solovev, K.; Golovin, A.; Dymshits, A. Composition of the kimberlite melt of the Komsomolskaya-Magnitnaya pipe (Upper Muna field, Siberian craton). In Proceedings of the EGU General Assembly 2022, Vienna, Austria, 23–27 May 2022; p. 10980.
168. Pokhilenko, L.N.; Golovin, A.V.; Sharygin, I.S.; Pokhilenko, N.P. Accessory minerals of mantle xenoliths: First finds of Cl-free K-Fe sulfides. *Dokl. Earth Sci.* **2011**, *440*, 1404–1409. [[CrossRef](#)]
169. Sharygin, I.S.; Golovin, A.V.; Pokhilenko, N.P. Djerfisherite in xenoliths of sheared peridotite in the Udachnaya-East pipe (Yakutia): Origin and relationship with kimberlitic magmatism. *Russ. Geol. Geophys.* **2012**, *53*, 247–261. [[CrossRef](#)]
170. Sharygin, I.S.; Golovin, A.V.; Korsakov, A.V.; Pokhilenko, N.P. Tychite in mantle xenoliths from kimberlites: The first find and a new genetic type. *Dokl. Earth Sci.* **2016**, *467*, 270–274. [[CrossRef](#)]
171. Podborodnikov, I.V.; Shatskiy, A.; Arefiev, A.V.; Litasov, K.D. Phase relations in the system $\text{Na}_2\text{CO}_3\text{--CaCO}_3\text{--MgCO}_3$ at 3 GPa with implications for carbonatite genesis and evolution. *Lithos* **2019**, *330–331*, 74–89. [[CrossRef](#)]
172. Safonov, O.G.; Shiryaev, A.A.; Tyurnina, A.V.; Huthwelker, T. Structural features of quench products of melts in the chloride-carbonate-silicate systems revealed by vibrational and X-ray spectroscopy. *Petrology* **2017**, *25*, 23–41. [[CrossRef](#)]
173. Evans, B.W.; Johannes, W.; Oterdoom, H.; Trommsdorff, V. Stability of chrysotile and antigorite in serpentinite multisystem. *Schweiz. Mineral. Petrogr. Mitt.* **1976**, *56*, 79–93.
174. Ulmer, P.; Trommsdorff, V. Serpentine Stability to Mantle Depths and Subduction-Related Magmatism. *Science* **1995**, *268*, 858–861. [[CrossRef](#)]
175. Evans, B.W. The Serpentine Multisystem Revisited: Chrysotile Is Metastable. *Int. Geol. Rev.* **2004**, *46*, 479–506. [[CrossRef](#)]
176. Doucet, L.S.; Ionov, D.A.; Golovin, A.V.; Pokhilenko, N.P. Depth, degrees and tectonic settings of mantle melting during craton formation: Inferences from major and trace element compositions of spinel harzburgite xenoliths from the Udachnaya kimberlite, central Siberia. *Earth Planet. Sci. Lett.* **2012**, *359–360*, 206–218. [[CrossRef](#)]
177. Ionov, D.A.; Liu, Z.; Li, J.; Golovin, A.V.; Korsakov, A.V.; Xu, Y. The age and origin of cratonic lithospheric mantle: Archean dunites vs. Paleoproterozoic harzburgites from the Udachnaya kimberlite, Siberian craton. *Geochim. Cosmochim. Acta* **2020**, *281*, 67–90. [[CrossRef](#)]
178. Maas, R.; Kamenetsky, M.B.; Sobolev, A.V.; Kamenetsky, V.S.; Sobolev, N.V. Sr, Nd, and Pb isotope evidence for a mantle origin of alkali chlorides and carbonates in the Udachnaya kimberlite, Siberia. *Geology* **2005**, *33*, 549–552. [[CrossRef](#)]
179. Kamenetsky, V.S.; Kamenetsky, M.B.; Sharygin, V.V.; Golovin, A.V. Carbonate-chloride enrichment in fresh kimberlites of the Udachnaya-East pipe, Siberia: A clue to physical properties of kimberlite magmas? *Geophys. Res. Lett.* **2007**, *34*, L09316. [[CrossRef](#)]
180. Kamenetsky, V.S.; Kamenetsky, M.B.; Golovin, A.V.; Sharygin, V.V.; Maas, R. Ultrafresh salty kimberlite of the Udachnaya-East pipe (Yakutia, Russia): A petrological oddity or fortuitous discovery? *Lithos* **2012**, *152*, 173–186. [[CrossRef](#)]
181. Kitayama, Y.; Thomassot, E.; Galy, A.; Golovin, A.; Korsakov, A.; d'Eyrames, E.; Assayag, N.; Bouden, N.; Ionov, D. Co-magmatic sulfides and sulfates in the Udachnaya-East pipe (Siberia): A record of the redox state and isotopic composition of sulfur in kimberlites and their mantle sources. *Chem. Geol.* **2017**, *455*, 315–330. [[CrossRef](#)]
182. Kitayama, Y.; Thomassot, E.; Galy, A.; Korsakov, A.; Golovin, A.; d'Eyrames, E. Geochemical evidence for carbon and chlorine enrichments in the mantle source of kimberlites (Udachnaya pipe, Siberian craton). *Geochim. Cosmochim. Acta* **2021**, *315*, 295–316. [[CrossRef](#)]
183. Boyd, F.R.; Pokhilenko, N.P.; Pearson, D.G.; Mertzman, S.A.; Sobolev, N.V.; Finger, L.W. Composition of the Siberian cratonic mantle: Evidence from Udachnaya peridotite xenoliths. *Contrib. Mineral. Petrol.* **1997**, *128*, 228–246. [[CrossRef](#)]
184. Keppler, H. Water solubility in carbonatite melts. *Am. Mineral.* **2003**, *88*, 1822–1824. [[CrossRef](#)]
185. Jacobson, N.S.; Fegley, B., Jr.; Setlock, J.A.; Costa, G. Solubility of Water in Carbonatites. *ACS Earth Space Chem.* **2020**, *4*, 2144–2152. [[CrossRef](#)]
186. Kavanagh, J.L.; Sparks, R.S.J. Temperature changes in ascending kimberlite magma. *Earth Planet. Sci. Lett.* **2009**, *286*, 404–413. [[CrossRef](#)]
187. Dawson, J.B.; Garson, M.S.; Roberts, B. Altered former alkalic carbonatite lava from Oldoinyo Lengai, Tanzania: Inferences for calcite carbonatite lavas. *Geology* **1987**, *15*, 765–768. [[CrossRef](#)]
188. Zaitsev, A.N.; Keller, J. Mineralogical and chemical transformation of Oldoinyo Lengai natrocarbonatites, Tanzania. *Lithos* **2006**, *91*, 191–207. [[CrossRef](#)]
189. Goryainov, S.V.; Krylova, S.N.; Borodina, U.O.; Krylov, A.S. Dynamical Immiscibility of Aqueous Carbonate Fluid in the Shortite–Water System at High-Pressure–Temperature Conditions. *J. Phys. Chem. C* **2021**, *125*, 18501–18509. [[CrossRef](#)]

Disclaimer/Publisher’s Note: The statements, opinions and data contained in all publications are solely those of the individual author(s) and contributor(s) and not of MDPI and/or the editor(s). MDPI and/or the editor(s) disclaim responsibility for any injury to people or property resulting from any ideas, methods, instructions or products referred to in the content.